

INSTITUTE
FOR
AEROSPACE STUDIES

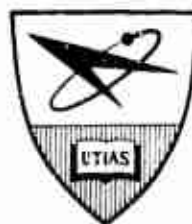
UNIVERSITY OF TORONTO

AD694506

BENDING RESPONSE OF A CANTILEVER CYLINDER TO TURBULENT SHEAR FLOW

by

K. R. Cooper



August, 1969.

UTIAS Technical Note No. 130

BENDING RESPONSE OF A CANTILEVER CYLINDER TO TURBULENT SHEAR FLOW

by

K. R. Cooper

Manuscript received May, 1969.

August, 1969.

UTIAS Technical Note No.139

ii ACKNOWLEDGEMENT

The work reported herein was supported by a National Research Council Grant, and by the Flight Dynamics Laboratory of the USAF Research and Technology Division, contract number F 33615-68-C-1055.

I would also like to thank the staff and students of UTIAS for their invaluable assistance and, in particular, Prof. B. Etkin, Mr. D. Surry, Mr. L. Reid and Mr. M. Gordon-Smith.

SUMMARY

This report describes a continuation of the work reported in NACA Technical Note by A. C. Campbell and B. Etkin titled "The Response of Cylindrical Structure to a Turbulent Flow Field at Subcritical Reynolds Number". Their model, suitably modified, was used for the present analysis.

The response of the base bending moment of a slender, vertically-mounted cantilever cylinder to a turbulent flow field with shear was measured for the drag (streamwise) and lift directions, and the drag response was compared to the response calculated for the same flow field by a linear theory due to B. Etkin.

This theory makes use of the method of normal modes, and includes only the effect of random turbulence in the generalized force function. The turbulent field was determined by measurement of the requisite space-time correlations.

Agreement between the theoretical predictions and experimental measurements was found to be quite good, especially at lower frequencies.

TABLE OF CONTENTS

	<u>PAGE</u>
NOTATION	
INTRODUCTION	
1. EXPERIMENT AND ANALYSIS	1
1.1 Model	1
1.2 Instrumentation	2
1.3 Mount and Installation	2
1.4 Scaling	2
1.5 Theoretical Bending Moment Spectrum	3
1.6 Theoretical Mean Bending Moment	5
1.7 Experimental Bending Moment Spectra	6
2. TURBULENCE DATA	7
2.1 Measurement of Cross-Correlation Tensor	7
2.2 Turbulence Spectra	9
2.3 Scale of Turbulence	10
3. EXPERIMENTAL RESULTS	11
3.1 Mean Bending Moment	11
3.2 Spectral Response	11
4. THEORETICAL RESULTS	12
4.1 Mean Bending Moment	12
4.2 Spectral Response	12
5. COMPARISON OF THEORY AND EXPERIMENT	13
6. CONCLUSIONS	15
REFERENCES	17
APPENDIX A - Statistical Specifications of the Turbulent Field	
APPENDIX B - Structural Response	
APPENDIX C - System Parameters	
APPENDIX D - Errata for Previous Report	
FIGURES	

NOTATION

b	local width of structure
B	stiffness, $B = EI$
C_a	aerodynamic damping coefficient per unit length
C_d	local drag coefficient per unit length
$D(\tau)$	Hanning lag window
E	modulus of elasticity
\bar{f}	reduced frequency
f	frequency, cps
f_n	undamped natural frequency of nth mode
l_1	Appendix B, Eq. (b6)
l_2	Appendix B, Eq. (b7)
$\mathcal{F}_n(t)$	generalized force in the nth mode
$F_n(z)$	shape of the nth mode
$F_n''(z)$	$d^2 F_n(z)/dz^2$
g_n, h_n	Appendix B, Eqs. (b19), (b20)
$G_n(if)$	transfer function
$G_n^*(if)$	complex conjugate of transfer function
I_n	generalized inertia in the nth mode, Appendix A, Eq. (15)
I	moment of inertia of model cross-section
k	local additional-mass coefficient
l	model length
l'	exposed model length
$L_x(z)$	longitudinal scale of turbulence
$L_z(z)$	lateral scale of turbulence
M	bending moment
m	mass per unit length of structure

m'	mass per unit length of structure, including "additional" mass
m, n	mode numbers
$q_n(t)$	tip deflection of nth mode
$Q(f)$	Hanning spectral window
$R_{uu}(\alpha, \beta, \tau)$	velocity cross-correlation function for a time delay τ
$\hat{R}_{uu}(\alpha, \beta, \tau)$	measured velocity cross-correlation function
$\tilde{R}_{uu}(\alpha, \beta, \tau)$	modified measured velocity cross-correlation function
R_1	even part of cross-correlation
R_2	odd part of cross-correlation
R	normalized co-spectrum
S	Strouhal number
t	time; wall thickness
T	averaging time
$U(z, t)$	horizontal wind velocity
$\bar{U}(z)$	time average of U at fixed z
$u(z, t)$	turbulent component of $U(z, t)$
\bar{u}	rms value of turbulent component
$W(z, t)$	force per unit length on the structure
$\bar{W}(z)$	time average of $W(z, t)$
$w(z, t)$	fluctuating part of $W(z, t)$
$w'(z, t)$	the part of w associated with the turbulence
x	wind tunnel axial co-ordinate
$X(z, t)$	total deflection of structure
$x(z, t)$	fluctuating part of $X(z, t)$
$\bar{X}(z)$	time average of $X(z, t)$
α, β	dummy variables of integration, denoting position on z axis
$\phi(f)$	spectrum function

$\phi_{\mathcal{F}_n \mathcal{F}_m}(f)$	cross spectrum function of the nth and mth generalized forces
$\phi_{BM}(z, f)$	power spectrum function of the bending moment at z
$\phi_{uu}(\alpha, \beta, f)$	cross spectrum function of longitudinal velocity at any two positions α and β (Power spectrum for $\alpha = \beta$)
$\phi_{xx}(z, f)$	power spectrum function of lateral displacement at z
ϕ_1	real component of velocity cross-spectrum function
ϕ_2	imaginary component of velocity cross-spectrum function
ζ_{Tn}	damping ratio of nth mode
ρ	air density
ζ_{a_n}	aerodynamic damping ratio
ζ_{s_n}	structural damping ratio
λ_n	narrow band turbulence
η	strain gauge calibration slope
σ^2	variance of any statistical process
τ	lag time
$()^T$	truncated value
$()_D$	drag component
$()_L$	lift component
$()_{UF}$	unfiltered computed value
$()_F$	filtered computed value
$()_{EXP}$	experimental value

INTRODUCTION:

Considerable interest has been shown, in recent years, in the response of tall, slender structures (radio antennae, tall towers, smoke stacks, launch vehicles, etc) to random excitation by atmospheric turbulence.

The response to any such excitation is also random and so must be treated in a statistical manner. This response can be described in terms of either a spectral density function (in the frequency domain) or a correlation function (in the time domain). Following usual practice, the response analysis is expressed in the frequency domain.

This report compares the computed spectral density with the measured spectral density of the drag response for a thin-walled uniform brass cylinder which has mechanical and aerodynamic properties similar to the contemporary slender structures mentioned above.

The turbulent stream can be looked upon as consisting of two components, one static and one dynamic. That is, we have an oscillating turbulent velocity component superimposed on some mean flow. In this case, to provide a better test of the mathematical model proposed, a non-uniform mean velocity profile (shear profile) was employed. The shear turbulent flow field was developed behind a "shear" grid (see Fig.1) and its mean velocity profile is shown in Fig.2, while the associated turbulent component is recorded in Fig.3.

The turbulence properties were initially determined in the time domain, because the availability of a correlation function computer (PAR MODEL 100) made these measurements most expedient. A digital Fourier transformation of these correlations was employed to generate the corresponding spectrum functions.

Just as the flow field consists of a static and dynamic component so the bending response of the beam in the drag direction has a mean and a time varying component. It is this fluctuating drag component that is of primary interest.

1. EXPERIMENT AND ANALYSIS

1.1 Model

The thin-walled brass cylinder (see Fig.4) used for the model originally had the following dimensions (ex Campbell model, reference 3).

Length	29.5 inches
Diameter	.45 inches
Wall thickness	.010 inches

Initial measurements, however, showed that the structural damping was lower than wanted ($\xi_s = .001$), so an outer sheath of visco-elastic material was heat shrunk onto the cylinder (see Fig.4). This modification more than doubled the structural damping ($\xi_s = .0022$), yet did not increase bending stiffness measurably. The final dimensions of the model were

Length	29.5 inches
--------	-------------

Diameter	.50 inches
Wall thickness	.026 inches

1.2 Instrumentation

The principal instrumentation used to obtain the bending response data was strain gauges. Two four-gauge bridges, with one gauge per bridge arm, were mounted on the model near the base (see Fig.5). The gauges were powered by a 12 volt d.c. source and their outputs were multiplied by a gain of 500 in highly accurate differential amplifiers. The output from 20 cps to 500 cps, the upper portion of the range of interest, was analyzed on line. The lift signal (with zero mean) was frequency analyzed directly by a Bruel and Kjaer wave analyzer and random noise meter, while the drag signal first had the mean signal removed (and recorded) before frequency analysis.

The wave analyzer was of the constant percent bandwidth type, and the bandwidth used was the most narrow (7.5 percent). The random noise meter was equipped with a variable time-constant and was used to obtain the true rms signal from the wave analyzer, whose low frequency capability extended to 20 cps.

Because analysis was required down to as low a frequency as possible, some data was tape recorded at 1-7/8 ips on an Ampex SP 300 recorder. By playing this record back at 15 ips, analysis was possible down to 2.5 cps. In this manner a frequency range from 2.5 to 500 cps was attained.

1.3 Mount and Installation

Care was required in the manner of supporting the model so that extraneous vibrations in the frequency band of interest would be eliminated. Campbell's mount was used as it was entirely adequate.

A 30 pound weight was supported by four thin steel rods (1/8 inch diameter) as shown in Fig.6, and the cylinder was fastened to the weight. The natural frequency of the mount was 1.3 cps.

The mount was then isolated from the wind tunnel by being supported directly from the concrete floor beneath the tunnel (see Fig's. 6 and 7).

A large fairing with an attached ground board was used to shield the weight from the flow, and to remove the effects of the tunnel boundary layer. The fairing was so arranged that the lower portion of the cylinder on which the strain gauges were mounted was also shielded, so that exactly 27.0 inches of the cylinder extended above the ground board (see Fig.8).

The cylinder was located in the diffuser section downstream of the test section, 125 inches from the shear grid. The tunnel aerodynamic outline is shown in Fig.9 and the grid and test location are both indicated.

1.4 Scaling

The requirements for dynamic and geometric similarity of an aeroelastic model, from dimensional analysis, were found to be

ζ_{T_n}	total damping ratio
$Et/\rho \bar{U}^2 b$	elasticity parameter
$m/\rho b^2$	density parameter
$\rho \bar{U} b/\mu$	Reynold's number
L_x/b	Flow structure
b/ℓ	Geometric similarity

where the model and full size structure must have the same values of the above parameters.

Assuming the same mean velocity profile for both model and full scale (no attempt was made to scale the earth's boundary layer) then the model represents one possible steel structure of the following dimensions -

length	216 feet
diameter	4.0 feet
wall thickness	.5 inches

1.5 Theoretical Bending Moment Spectrum (after Campbell & Etkin)

Appendix B gives the general theory, and by using some simplifying assumptions the theory was applied to the cylindrical model.

The basic deflection spectral relation is given by (b21) as

$$\phi_{xx}(z, if) = \sum_{m=1}^{\infty} \sum_{n=1}^{\infty} F_m(z) F_n(z) G_m^*(if) G_n(if) \phi_{\mathcal{F}_m \mathcal{F}_n}(f) \quad (1.5.1)$$

where $F_m(z)$, $F_n(z)$ are the mode shape functions; $G_m(if)$, $G_n(if)$ are the transfer functions (* indicates the complex conjugate) for the mth and nth modes and $\phi_{\mathcal{F}_m \mathcal{F}_n}(f)$ is the generalized input force cross spectrum function.

For the case of a lightly damped system (which we have), and for a structure whose natural mode frequencies are well separated we can assume that there is no cross coupling between modes of the model. Thus

$$\phi_{\mathcal{F}_m \mathcal{F}_n}(f) = 0$$

for $m \neq n$. Hence the above equation reduces to

$$\phi_{xx}(z, if) = \sum_{n=1}^{\infty} F_n^2(z) \left| G_n(if) \right|^2 \phi_{\mathcal{F}_n \mathcal{F}_n}(f) \quad (1.5.2)$$

The bending moment-deflection relation is

$$M(z, +) = B(z) \partial^2 x / \partial z^2 \quad (1.5.3)$$

where $B(z) = EI(z) = \text{constant}$. But from the modal representation of deflection

$$x(z,t) = \sum_n F_n(z) q_n(t) \quad (1.5.4)$$

Hence

$$\partial^2 x / \partial z^2 = \sum_n \frac{d^2 F_n(z)}{dz^2} q_n(t)$$

$$\text{i.e.,} \quad \partial^2 x / \partial z^2 = \sum_n F_n''(z) q_n(t)$$

For the case of base bending moment

$$\left. \frac{\partial^2 x}{\partial z^2} \right|_{z=0} = \sum_n F_n''(0) q_n(t) \quad (1.5.5)$$

Using (1.5.3) and (1.5.5) the bending moment spectrum may be expressed

$$\phi_{BM}(f) = \sum_n B^2 F_n''(0) \left| G_n(if) \right|^2 \phi_{\mathcal{J}_n \mathcal{J}_n}(f) \quad (1.5.6)$$

The values of B , $F_n''(0)$ and $|G_n(if)|^2$ are given in Appendix C. The generalized force spectrum $\phi_{\mathcal{J}_n \mathcal{J}_n}(f)$ is given by equation (b 25) and is for this case

$$\begin{aligned} \phi_{\mathcal{J}_n \mathcal{J}_n}(f) = & \int_0^{L'} \int \phi_{uu}(\alpha, \beta, f) \left\{ g_n(\alpha) g_n(\beta) + 4\pi^2 f^2 h_n(\alpha) h_n(\beta) \right. \\ & \left. + i 2 \pi f [g_n(\alpha) h_n(\beta) - g_n(\beta) h_n(\alpha)] \right\} d\alpha d\beta \end{aligned} \quad (1.5.7)$$

Now consider the integrals over the (α, β) domain illustrated in Fig. 10. Let the integrals be evaluated by summing at pairs of elements (p, q) that are symmetric with respect to the diagonal. Since (α, β) are interchanged at p and q , the following relations hold

$$\left. \begin{array}{l} g_n(\alpha) g_n(\beta) \\ h_n(\alpha) h_n(\beta) \end{array} \right\} \text{at } p = \left. \begin{array}{l} g_n(\alpha) g_n(\beta) \\ h_n(\alpha) h_n(\beta) \end{array} \right\} \text{at } q \quad (1.5.8)$$

Using these relations plus the symmetry relations (a 16) and (a 17) and equation (a 11) (which separates $\phi_{uu}(\alpha, \beta, f)$ into real and imaginary parts) in equation (1.5.7), we obtain the generalized force spectrum function

$$\begin{aligned} \phi_{\mathcal{J}_n \mathcal{J}_n}(f) = & \int_0^{L'} \int \left\{ \phi_1(\alpha, \beta, f) [g_n(\alpha) g_n(\beta) + 4\pi^2 f^2 h_n(\alpha) h_n(\beta)] \right. \\ & \left. + 2\pi f \phi_2(\alpha, \beta, f) [g_n(\alpha) h_n(\beta) - g_n(\beta) h_n(\alpha)] \right\} d\alpha d\beta \end{aligned} \quad (1.5.9)$$

Where l' is the exposed length (27.0 inches) of the cylinder and ϕ_1 and ϕ_2 are the real and imaginary components of the velocity spectrum function. An estimate of the true velocity cross spectrum is required to evaluate (1.5.9).

At this point two assumptions which have been important in the development of the theory should be emphasized.

- (i) The structure is sufficiently slender for the secondary span-wise flow and consequent redistribution of pressures to be neglected, such that the pressures on any section of the span are only due to the wind incident on that section. This is the "strip theory" assumption.
- (ii) The turbulent fluctuations are so small compared to the mean velocity that the fluctuating loads can be expressed as linear functions of the turbulent velocities.

Both of these will be discussed in section 2. Assuming two-dimensional flow over a large portion of such a long slender cylinder the drag coefficient chosen was (Ref.15)

$$C_D = 1.2$$

1.6 Theoretical Mean Bending Moment

The force per unit length on the cylinder due to the mean flow at position z is

$$f(z) = \frac{C_D \rho b}{2} \bar{U}^2(z) \quad (1.6.1)$$

Thus the force on the increment dz at z is

$$dF_z = f(z) dz = \frac{C_D \rho b}{2} \bar{U}^2(z) dz \quad (1.6.2)$$

The bending moment due to the force on the increment dz at z is

$$dM = dF_z z = \frac{C_D \rho b}{2} \bar{U}^2(z) z dz \quad (1.6.3)$$

Hence the total mean bending moment is

$$\bar{M} = \frac{C_D \rho b}{2} \int_{2.5}^{29.5} \bar{U}^2(z) z dz \quad (1.6.4)$$

The limits are due to the fact that not all of the cylinder is exposed, so \bar{U} below $z = 2.5$ inches is zero.

1.7 Experimental Bending Moment Spectra

The experimental bending moment spectra can be found from the rms output of the wave analyzer. The filter characteristic of the wave analyzer for sine wave inputs at frequency f is shown in Fig.11.

$$g(f/f_s) = \frac{\text{mean square output}}{\text{mean square input}} = \frac{\overline{e_o^2}}{\overline{e_i^2}} \quad (1.7.1)$$

where f_s is the centre frequency. Then the mean square output signal from the wave analyzer is

$$\overline{e_o^2}(f, f_s) = g(f/f_s) \overline{e_i^2}(f) \quad (1.7.2)$$

Now the strain gauge signal, e_i (see Fig.67), is directly proportional to the base bending moment, i.e.,

$$e_i = \eta M \quad (1.7.3)$$

and

$$\overline{e_i^2} = \eta^2 \overline{M^2} \quad (1.7.4)$$

where η is the slope of the strain gauge calibration curves (see Fig.12). Thus the wave analyzer output signal is

$$\overline{e_o^2}(f, f_s) = g(f/f_s) \eta^2 \overline{M^2} \quad (1.7.5)$$

But from the bending moment spectrum curve the mean square bending moment about the mean, for a wide-band input is

$$\overline{M^2} = 2 \int_0^\infty \phi_{BM}(f) df \quad (1.7.6)$$

Thus the output corresponding to the wave-analyzer centre frequency f_s is

$$\overline{e_o^2}(f_s) = 2 \eta^2 \int_0^\infty \phi_{BM}(f) g(f/f_s) df \quad (1.7.7)$$

Assuming $\phi_{BM}(f)$ is approximately constant over the frequency band of the filter, (1.7.7) becomes

$$\overline{e_o^2}(f_s) = 2 \eta^2 \phi_{BM}(f_s) \int_0^\infty g(f/f_s) df \quad (1.7.8)$$

Let

$$\int_0^\infty g(f/f_s) d(f/f_s) = G \quad (1.7.9)$$

Then

$$2 \phi_{BM}(f) = \overline{e_o^2} (f_s) / \eta^2 f_s G \quad (1.7.10)$$

For the filter used $G = .0763$.

The mean bending moment is obtained from the mean voltage output as developed in the analogue analysis.

2. TURBULENCE DATA

2.1 Measurement of $R_{uu}(\alpha, \beta, \tau)$

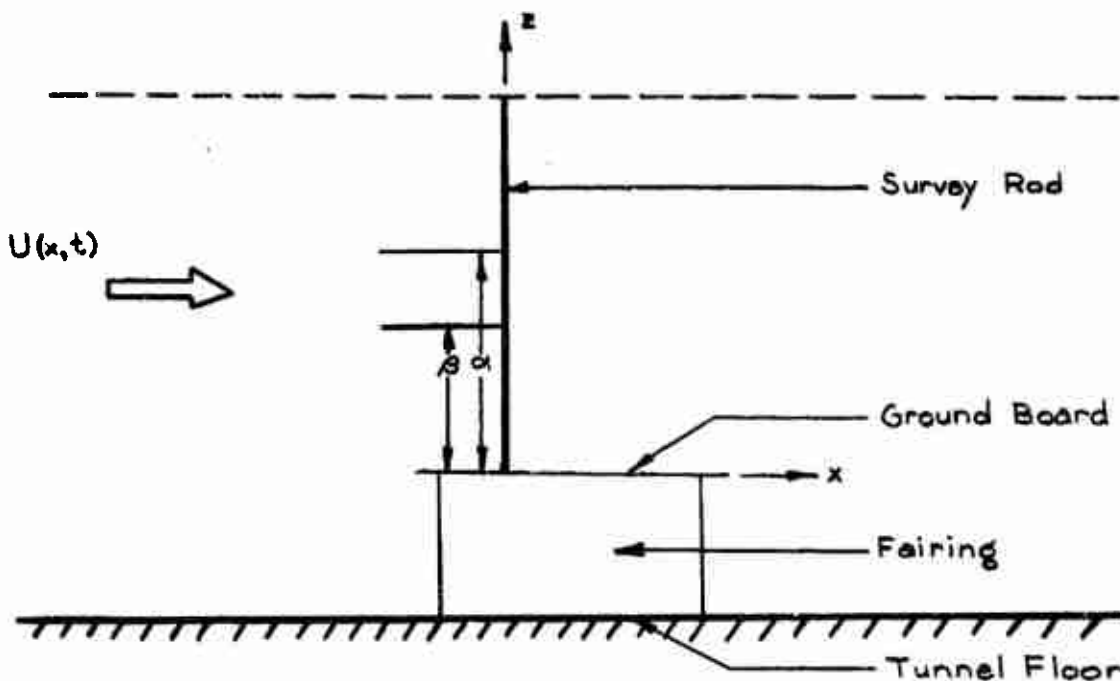
The turbulent flow field was developed behind a shear grid (Fig.1) in the UTIAS Subsonic Wind Tunnel.

The initial survey was carried out using a single hot wire probe, ranged in increments of 1 inch from the ground board ($z = .125$ in) to $z = 30$ in. Employing the analogue computation scheme shown in Fig.13, (mechanized on the UTIAS PACE computer) the mean was extracted from the signal and displayed on a digital voltmeter, while the rms value of the fluctuating component was measured by a Bruel and Kjaer random noise meter. The linearized hot wire output was converted to velocity using the calibration curve, Fig.14. The resulting mean velocity and turbulence intensity profiles are shown in Fig's. 2 and 3 respectively. (Figure 27 shows Reynolds number).

The turbulence intensity over the first 6-8 inches of the cylinder seems too high for the linear assumption (ii) of (1.5) to hold. However, a constant temperature anemometer tends to over estimate the intensity (see Ref.4) of high intensity turbulence so the real case is not as bad as first appears. Also this phenomenon occurs over the lower portion of the cylinder where the drag and contribution to the bending moment are small so the error incurred would be small if assumption (ii) is retained.

One other result of such high intensities is that reverse flow, which the probe cannot separate from forward flow, is possible part of the time, but this effect is small also. For example (assuming a normal distribution for $u(x,t)$ at $z = 3$ inches, the probability of being within $2\sigma = 2\overline{u}/\overline{U} = 1.0$ is 95.4%. Thus reverse flow occurs only 2.3% of the time. At $z = 8$ inches the probability of reverse flow is only .15% and at $z = .125$ inches the probability is 21.5%. Obviously this has little or no effect on the response.

For the cross correlation measurements (see Appendix A1), two probes were required (see Fig.15). The signals from these probes first had the mean components removed (as above) and were then fed into a Princeton Applied Research Correlation Function Computer (Model 100). The probe arrangement and notation used, is diagrammed below.



Probe α is the fixed probe, while probe β ranges around each α position. Increments in α and β of 2.7 inches were used for a survey range of .125 (as close to the ground board as possible) to 27.0 inches (i.e., .125, 2.7, 5.4, ..., 27.0).

The PAR computer calculates the correlation function for 100 points at lag increments of $\tau_{\max}/100$, where τ_{\max} is the maximum lag time chosen. This choice is based on both required frequency response, and the desire to include the whole correlation curve. A value of $\tau_{\max} = .2$ sec ($\Delta\tau = .002$ sec) was chosen as this provided a frequency cutoff at 250 cps. which covered the first three bending modes, and included the majority of the correlation curve. The averaging time for the computer was 40 seconds. The correlation function computed may be written

$$\hat{R}_{uu}(\alpha, \beta, \tau) = \frac{1}{40} \int_0^{40} u(\alpha, t) u(\beta, t + .002 n) dt \quad (2.1.1)$$

where $n = 1, 2, \dots, 100$ (i.e., $\tau = 0, .002, \dots, .2$ sec). As can be seen from equation (a 18) this is only one half of the total cross correlation. By reversing the probe inputs to the PAR computer we get from (2.1.1).

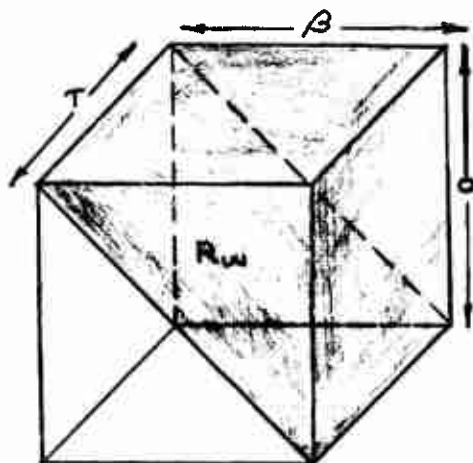
$$\hat{R}_{uu}(\beta, \alpha, \tau) = \frac{1}{40} \int_0^{40} u(\beta, t) u(\alpha, t + .002 n) dt \quad (2.1.2)$$

However, applying the symmetry properties (a 14) and (a 15) to (2.1.2) we see that

$$\hat{R}_{uu}(\beta, \alpha, \tau) = R_{uu}(\alpha, \beta, -\tau) \quad (2.1.3)$$

Thus by reversing the inputs, the second half of the correlation curve was obtained.

These symmetry properties were also used to reduce the number of measurements required. From (2.1.3) we can see that reversing the time scale for a fixed (α, β) relationship gives the cross correlation for the (β, α) input. Instead of having to measure the entire tensor shown below, we only need measure the shaded half.



Figures 16 to 26 show a typical set of correlation curves, obtained for $\alpha = 13.5$ inches and β ranging from .125 inches to 27.0 inches (the .125 inch value is considered zero).

2.2 Turbulence Spectra

The velocity cross correlations $\hat{R}_{uu}(\alpha, \beta, \tau)$ were Fourier transformed as in equations (a 12) and (a 13) and modified (Hanning factor, equations (a 26) applied) digitally as described in Appendix A.2. The transformed spectra corresponding to the correlations shown in figures 16 to 26 are shown in figures 28 to 38.

The total array of velocity cross spectra was employed with equation (1.5.9) to calculate the generalized input force spectra for each particular mode. Simpson's rule integration was employed in the digital program and should provide sufficient accuracy. The resulting inputs can be seen in figure 39. They demonstrated the form to be expected. The first mode input has the greatest content at low frequencies and drops off most rapidly with frequency. The second mode input is intermediate in magnitude and frequency range, while the third mode forcing function has the lowest content at low frequencies, but has the largest high frequency components.

Unfortunately all the signals disappeared at the noise level around 90 to 125 cps, so the third mode peak for the bending moment spectrum could not be calculated.

Also due to the finite maximum lag time available, some of each correlation curve was lost, and in spite of the Hanning correction, the low

frequency values will consequently be somewhat low.

Some workers (references 5 and 6) have used a coherence function (normalized co-spectrum) to calculate the cross spectral densities given the spatial distribution of velocity power spectral densities. They have assumed that

$$R = \phi_1(\alpha, \beta, f) / [\phi_{uu}(\alpha, \alpha, f) \phi_{uu}(\beta, \beta, f)]^{\frac{1}{2}} \quad (2.2.1)$$

when plotted versus

$$\bar{f} = f \Delta z / \frac{1}{2} (\bar{U}_\alpha + \bar{U}_\beta) \quad (2.2.2)$$

may be expressed in the form

$$R = e^{-k\bar{f}}$$

where k is some constant value which depends on the turbulent field.

Vickery (reference 6) quotes a value of $k = 9$ for rolling wooded country, and Davenport (reference 5) quotes $k = 6$ for wooded countryside (after Singer) and 7.7 for open grassland.

Figure 40 presents some of the turbulence data for various probe stations plotted in the form given by equations (2.2.1) and (2.2.2). The curve fitted through the points closely approximates

$$R = e^{-6.65 \bar{f}}$$

This approximation would seem of considerable value as it greatly reduces the work required to estimate the cross spectra.

The power spectra could be measured directly and it is felt that any errors incurred in the exponential approximation (2.2.3) would be outweighed by the very good accuracy achievable in the measurement of the power spectra, as compared to first obtaining the correlation, and then transforming to the frequency domain.

2.3 Scale of Turbulence (see Appendix A.3)

$$\text{The ratios } \frac{\hat{R}_{uu}(\alpha, \beta, 0)}{\hat{R}_{uu}(\alpha, \alpha, 0)} \quad (2.3.1)$$

which represent the normalized cross correlations are plotted versus probe separation $(\alpha - \beta)$ for all eleven survey positions in Figs. 41 to 51. The areas under these curves represent the lateral integral scales $L_y(z)$ given by equation (a 28). The distribution of scale over the cylinder length is shown in Fig. 52.

The longitudinal scale given by equation (a 28) is computed (assuming Taylor's hypothesis) by finding the area under the autocorrelation curve

$$A(\alpha) = \int_0^\infty \hat{R}_{uu}(\alpha, \alpha, \tau) d\tau \quad (2.3.2)$$

and then multiplying by

$$\bar{U}(\alpha) / \hat{R}_{uu}(\alpha, \alpha, 0)$$

to normalize the correlation and convert to length units so that the result.

$$\frac{A(\alpha) U(\alpha)}{\hat{R}_{uu}(\alpha, \alpha, 0)}$$

corresponds to $L_x(z)$ (equation (a 27)). These are plotted versus z in Fig.53.

For isotropic flow, $L_x(z) = 2 L_z(z)$ (reference 10). This does not hold for the present anisotropic flow, as can be seen in Fig's. 52 and 53. Generally however, $L_x(z) > L_z(z)$ except at the base of the cylinder where the turbulence intensity is very high, and here $L_z(z) > L_x(z)$.

For similarity between model and full scale flows, the ratio

$$\left[\frac{L_x(z)}{b(z)} \right]$$

should be the same for model and structure.

Since no attempt was made to scale flows, this parameter has no application here other than to support the strip theory assumption which requires $L \gg b$.

3. EXPERIMENTAL RESULTS

3.1 Mean Bending Moment

The mean bending moment for the lift direction was zero, and that of the drag direction was found to be

$$\bar{M}_D = 3.20 \text{ in lb.}$$

3.2 Spectral Response

The response spectra were calculated as outlined in section 1.7. The lift response is shown in Fig.55. The magnitude of the third mode peak is significantly greater than that of the second mode due to vortex shedding. The variation with height of Strouhal shedding frequency, assuming that a Strouhal number of .2 is applicable to the situation, is shown in Fig.54. As can be seen, over the top half of the cylinder the shedding frequency ranges from 150 cps. to 250 cps. The third mode natural frequency is 213 cps., so this mode is very likely being excited by the vortex shedding. The variance of the lift signal was equivalent to

$$\sigma_L^2 = 1.18 (\text{in lb})^2$$

The drag response spectrum is given in Fig.56. As expected, the drag

response is greater than that in the lift direction, in spite of the vortex excitation. The variance for the drag signal was equivalent to

$$\sigma_D^2 = 6.17 (\text{in lb})^2$$

The ratios of peak values of the drag spectrum for the various modes are (order of magnitude only)

first to second	10^3
first to third	10^4
second to third	10^1

For the cases where vortex excitation was present Campbell obtained

first to second	10^3
first to third	10^4
second to third	10^1

When no vortex excitation was present the ratio "second to third" was approximately 10^2 .

This would suggest that as in the previous report, there is some cross-coupling between lift and drag in the third mode response.

4. THEORETICAL RESULTS

4.1 Mean Bending Moment

The mean bending moment was computed as shown in section 1.6., using a graphical evaluation of equation (1.6.4). The value obtained was

$$\bar{M}_D = 3.38 \text{ in lb.}$$

which is 5.8 percent higher than the measured value. The bending moment calculation was performed for a structure perpendicular to the mean flow. Actually there would be an equilibrium between the aerodynamic load and elastic restoring force, in which the structure would be deflected, and so the load on the curved cylinder would be slightly reduced due to the effective lowering of the normal flow velocity over the cylinder. (The magnitude of this effect was not, however, calculated).

4.2 Spectral Response

A digital program was written to evaluate equation (1.5.6) for $\phi_{BM}(f)$ using the generalized input force spectra calculated from equation (1.5.9).

The computed drag response is shown in Fig.57. However, this spectrum as it stands, was not felt to be sufficiently useful.

An assumption was made in the calculation of the experimental spectrum, that $\phi_{BM}(f)$ was constant over the bandwidth of the wave analyzer. Obviously,

this could not be true near a narrow response peak for a 7.5 percent bandwidth. Since the wave analyzer has a finite bandwidth, the spectrum at a particular frequency point is really an average over a frequency band around that frequency. This point would tend to confuse any direct comparison between theory and experiment for it would reduce experimental peak values, and increase the values between the peaks. As the point of this paper is just such a comparison, it was felt necessary to filter the computed data digitally, using the filter shape of the analyzer (Fig.11). Then the data would be directly comparable, and any discrepancies would not be due to the measurement and analysis technique of the experimentally obtained spectrum. The filtered theoretical drag spectrum is compared to the unfiltered spectrum in Fig.57.

One probable cause of the loss of the force spectrum above 100 cps. was an insufficiently high signal to noise ratio in the measurement of the turbulence. At the same time, other workers at the Institute have found that the validity of spectra obtained from the correlation function by Fourier transformation were unreliable once the spectrum was down from the peak value by three orders of magnitude. This is one of the reasons for the suggestion (section 2.2), that the exponential relation between power spectra and co-spectra be employed.

The variance for the frequency range of 2 cps to 100 cps. is

$$\left(\sigma_D^2 \right)_{\frac{T}{F}} = 6.43 \text{ (in lb)}^2$$

where the T superscript represents a "truncated" spectrum from 2 to 100 cps, and the subscript F represents the filtered computed response (see next section).

5. COMPARISON OF THEORY AND EXPERIMENT

Figure 56 directly compares the filtered theoretical and experimental drag bending moment spectra. The comparison is facilitated by reference to Fig.58, which gives a plot of the ratio of the filtered theoretical and experimental spectra. We can see that the agreement is reasonable (i.e., ratio reasonably close to 1.0) up to about 20 cps. but is poor at the highest frequencies. Surprisingly the theoretical values are lower than the experimental ones (one might expect larger values) except in the frequency ranges near the peaks, where the theoretical values are too high. This immediately suggests that the estimates of the generalized forces and the damping might have been in error.

Underestimation of the generalized force spectrum would lower the bending moment spectrum over the entire frequency range and partially account for the low portions between the peaks of Fig.56. However, near a peak, the damping term in the transfer function

$$1/64\pi^4 f^2 f_n^2 (\zeta_a^2 + \zeta_s^2)$$

dominates as f approaches f_n .

If the damping estimate were low, it would cause little change away from the peaks, but at a peak could significantly raise the peak value.

The structural damping was felt to be quite well defined, so any error in the damping is most likely due to the estimation of the aerodynamic part. Both the input force spectrum and the aerodynamic damping were based on the initial assumptions of strip theory and linearization. Certainly the linearization fails to some extent as does the two dimensional assumption, and so one would expect an erroneous theoretical estimate, though to the high side.

The agreement appears to fail progressively with increasing frequency. It is possible that the interaction of the flow with the more complex second mode shape causes some of the discrepancy. This could be readily determined by utilizing a stiffer cylinder whose first mode natural frequency would be in the neighbourhood of 75 cps.

It has been suggested above that -

- (i) the generalized force spectrum computed is too small in magnitude, especially for the second mode input.
- (ii) the aerodynamic damping is too small also.

Both these quantities are dependent on one very important parameter, the drag coefficient C_D . The value used was 1.2, which is typical of the flow Reynolds numbers (see Fig.27) for the uniform two dimensional flow expected over a large portion of such a long slender cylinder.

In a turbulent field a somewhat lower value might be expected. However Scruton (Ref.9) has shown that the drag coefficient of a long slender finite cylinder increases quite sharply, at least 25-30 percent, toward the tip. On the basis of this information, it is very possible that the drag coefficient has been underestimated, and as this has very important consequences, should be investigated more closely.

An increase in C_D would, of course, increase the generalized input force spectrum and so improve the agreement between theory and experiment away from the peaks. At the peaks, an increase in C_D would cause a decrease in the theoretically computed values. This occurs because, although the input forces are increased, the larger C_D leads to a relatively greater reduction in the transfer function, through the aerodynamic damping terms (see equation (5.1)).

For example, the ratios of the peak values for $C_D = 1.3$ to the peak values for $C_D = 1.2$ for the first 3 modes are

<u>Mode</u>	<u>Ratio</u>
1	.875
2	.950
3	.980

As might be expected, the C_D change has a smaller effect for the higher modes because the aerodynamic damping is a smaller and smaller component of the total damping.

Good agreement up to 50 cps. would require a value of C_D of about 1.45 to 1.50. However, no reasonable adjustment in C_D would correct for the total error at the second mode peak.

The data presented beyond 90 cps. was expected to be low, as the input force spectra were approaching noise level.

Table 3 provides a comparison of the contribution to the total variance, of various frequency bands of the filtered and unfiltered theoretical response, with the experimental response. The effect of filtering is seen as a small increase in the variance components resulting in a slightly higher filtered variance. (4%). These ratios were plotted in Fig. 59 and, of course, reflect the form of Fig. 56.

The total variance for the theoretical truncated filtered spectrum was found to be

$$\left[\sigma_D^2 \right]_F^T = 6.43 \text{ (in lb)}^2$$

and the variance for the truncated experimental spectrum was found to be

$$\left[\sigma_D^2 \right]_{EXP}^T = 5.99 \text{ (in lb)}^2$$

Vickery, reference 6, found that his computation for a somewhat similar case resulted in the theoretical variance being high by about 22.5%. In this case the theory is 8% high.

Again it should be pointed out that the discrepancy in the region of the second mode has not been explained, and it is suggested that this point be the subject of further research.

6.0 CONCLUSIONS

- (i) The theory provides a good description of the response of a slender structure to turbulence at the first mode for sufficiently low frequencies of vibration. The variance of the theoretically calculated response was eight percent higher than the measured value.
- (ii) At higher modes and/or for sufficiently high frequencies the theoretically predicted values of drag response are low. This discrepancy may be caused by some or all of -
 - a) Failure of the two-dimensional assumptions at higher frequencies
 - b) A low value of C_D , although no reasonable C_D value could explain the total discrepancy.
 - c) Some flow-response phenomenon of the higher modes not represented by the theory.
- (iii) The two-dimensional subcritical value assumed for the drag coefficient, $C_D = 1.2$, appears to be low.
- (iv) The overestimation of the response at the natural mode peaks may be due to a low estimate of aerodynamic damping which can be tied

to a low value of C_D . However, this does not explain the entire response at the second mode peak, and so it is possible that the value of structural damping for the second mode is in error.

- (v) The lift response to turbulence was shown to be considerably lower than the drag response.
- (vi) More work is required to determine the proper value (s) for C_D and to investigate the high frequency, higher mode response.

REFERENCES

1. Bendat, J. S.
Piersol. Measurement and Analysis of Random Data
2. Blackman, R. B.
Tukey. The Measurement of Power Spectra, Dover Publications Inc. 1958.
3. Campbell, A. C.
Etkin, B. The Response of A Cylindrical Structure to a Turbulent Flow Field at Subcritical Reynolds No. UTIAS Tech. Note.115, July 1967.
4. Hinze, J. O. Turbulence, McGraw-Hill, 1959.
5. Davenport, A. G. The Response of a Slender Line-Like Structure to a Gusty Wind, Proc. I.C.E., Vol.23, 1962.
6. Vickery, B. J. Wind Loads on Tall Stacks, A.M.S. Conference on Atmospheric Turbulence, 1968.
7. Etkin, B. Theory of the Response of a Slender Vertical Structure to a Turbulent Wind with Shear, Proc. of NASA meeting on Ground Wind Loads in Relation to Launch Vehicles, Langley Research Centre, June 1966.
8. Bisplinghoff, R. L.
Ashley, H.
Halfman, R. L. Aeroelasticity, Addison Wesley, Pbl. Co. 1957.
9. Scruton, C. Aerodynamics of Structures, Paper 4 Proc. of the International Research Seminar at the NRC, Ottawa 1967.
10. Batchelor, G. K. Homogeneous Turbulence, Cambridge University Press, 1953.
11. Townsend, A.A. Structure of Turbulent Shear Flow, Cambridge University Press, 1956.
12. Lin, C. C. Statistical Theories of Turbulence, Princeton University Press, 1961.
13. Handa, K. N. Response of Tall Structures to Atmospheric Turbulence, Institute of Sound and Vibrations Research, University of Southampton, December 1967.
14. Schubauer, G. B.
Tchen, C. M. Turbulent Flow, Princeton University Press, 1961.
15. Hoerner, S. F. Aerodynamic Drag, Atterbein Press, 1951.
16. Wardlaw, R. L.
Davenport, A. G. Some Experiments on the Fluctuating Forces on Flat Plates in Turbulent Flow.

APPENDIX A: STATISTICAL SPECIFICATION OF THE TURBULENT FIELD

1. FUNDAMENTALS (references 1,2,4,12,14)

The usual method of generating turbulence in a wind tunnel is to place a grid, or array of bars across the wind tunnel stream.

About 15 mesh diameters downstream of the grid, the turbulent field is fully developed, and at any point in the field the stream velocity can be seen to consist of a mean component and a component fluctuating about this mean (see Fig.60).

$$\text{i.e.,} \quad U(z,t) = \bar{U}(z) + u(z,t) \quad (a1)$$

To determine the field of turbulent motion statistically we require the system of complete joint probability distributions of the values of the turbulence velocity vectors, $u(z,t)$, at any n points of space-time.

Measurements are made by placing hot wire anemometer probes at fixed points relative to the grid and recording the variations with time of the linearized output. An average value of the required function of velocity is obtained by taking a mean value over a long period of time.

If we assume that the turbulence signal may be represented as a stationary Gaussian random process with zero averages (which it can if the mean value is subtracted from equation (a 1)), we may use this time average assuming ergodicity, to replace the probability average for the experimental field. Then all the relevant statistical information will be contained by the correlation function (or power spectrum).

As shown in Appendix B, a two point lateral space-time correlation tensor is required to evaluate the turbulent field, so this case will be discussed.

Consider two signals $u(\alpha,t)$, $u(\beta,t)$ from two probes at α and β (α and β are position coordinates) in the turbulent field. The cross-correlation for two such signals separated in time by the lag time τ , is defined as

$$R_{uu}(\alpha,\beta,\tau) = \lim_{T \rightarrow \infty} \frac{1}{2T} \int_{-T}^{+T} u(\alpha,t) u(\beta,t + \tau) dt \quad (a2)$$

where

$$R_{uu}(\alpha,\alpha,\tau) = \lim_{T \rightarrow \infty} \frac{1}{2T} \int_{-T}^{+T} u(\alpha,t) u(\alpha,t + \tau) dt \quad (a3)$$

is called the autocorrelation, and

$$R_{uu}(\alpha,\alpha,0) = \lim_{T \rightarrow \infty} \frac{1}{2T} \int_{-T}^{+T} u(\alpha,t) u(\alpha,t) dt \quad (a4)$$

is the variance of the process.

Equation (a2) may also be expressed as

$$R_{uu}(\alpha, \beta, \tau) = \int_{-\infty}^{\infty} \phi_{uu}(\alpha, \beta, f) e^{i2\pi f \tau} df \quad (a5)$$

where $\phi_{uu}(\alpha, \beta, f)$, the cross spectral density function, is given by

$$\phi_{uu}(\alpha, \beta, f) = \lim_{T \rightarrow \infty} \frac{1}{2T} \int_{-T}^T u(\alpha, t) u(\beta, t) e^{-i2\pi f t} dt \quad (a6)$$

The function $\phi_{uu}(\alpha, \alpha, f)$ is termed the "power spectrum", and $\phi_{uu}(\alpha, \alpha, f) df$ represents the contribution to the total variance of the portion of the signal in a frequency bandwidth of df at frequency f .

$$\text{i.e.,} \quad \int_{-\infty}^{\infty} \phi_{uu}(\alpha, \alpha, f) df = \sigma^2 \quad (a7)$$

The cross correlation and the cross spectrum form a Fourier transform pair, which may be expressed in a single-sided form as

$$R_{uu}(\alpha, \beta, \tau) = 2 \int_0^{\infty} \phi_{uu}(\alpha, \beta, f) e^{i2\pi f \tau} df \quad (a8)$$

$$\phi_{uu}(\alpha, \beta, f) = 2 \int_0^{\infty} R_{uu}(\alpha, \beta, \tau) e^{-i2\pi f \tau} d\tau \quad (a9)$$

The cross correlation function $R_{uu}(\alpha, \beta, \tau)$ for $u(x, t)$ is in general composed of parts that are even and odd in τ

$$\text{i.e.,} \quad R_{uu}(\alpha, \beta, \tau) = R_1(\alpha, \beta, \tau) + R_2(\alpha, \beta, \tau) \quad (a10)$$

where R_1 and R_2 are as in Fig.61. The corresponding spectrum function is

$$\phi_{uu}(\alpha, \beta, f) = \phi_1(\alpha, \beta, f) - i\phi_2(\alpha, \beta, f) \quad (a11)$$

where

$$\phi_1(\alpha, \beta, f) = 2 \int_0^{\infty} R_{uu}(\alpha, \beta, \tau) \cos 2\pi f \tau d\tau \quad (a12)$$

$$\phi_2(\alpha, \beta, f) = 2 \int_0^{\infty} R_{uu}(\alpha, \beta, \tau) \sin 2\pi f \tau d\tau \quad (a13)$$

The cross correlation is a mean lagged product of two signals, one advanced relative to the other. Obviously, for a statistically stationary processes, advancing the first is the same as delaying the second, so that interchanging the order is the same as changing the sign of τ . Accordingly we have the reciprocity properties

$$R_1(\alpha, \beta, \tau) = R_1(\beta, \alpha, -\tau) \quad (\text{a14})$$

$$R_2(\alpha, \beta, \tau) = -R_2(\beta, \alpha, -\tau) \quad (\text{a15})$$

The corresponding spectral relations are

$$\phi_1(\alpha, \beta, f) = \phi_1(\beta, \alpha, f) \quad (\text{a16})$$

$$\phi_2(\alpha, \beta, f) = \phi_2(\beta, \alpha, f) \quad (\text{a17})$$

2. PRACTICAL MEASUREMENT (reference 2)

To exactly determine the correlation function defined by (a2) a perfectly measured, infinitely long record of random data is needed. As this is obviously unobtainable, and in fact there is usually only a very limited amount of data available the estimate obtained for the correlation function will differ from the exact value. The estimated correlation function $R_{uu}(\alpha, \beta, \tau)$ at lag τ , may be expressed as

$$\hat{R}_{uu}(\alpha, \beta, \tau) = \frac{1}{2T} \int_{-T}^T u(\alpha, t) u(\beta, t + \tau) dt \quad (\text{a18})$$

where T is the averaging time and τ is the lag to be used.

Not only is this estimated correlation function truncated relative to the exact function, but for the lag times available, it will also possess different magnitudes as a result of the finite averaging time although due to ergodicity

$$1. \quad \langle \hat{R}_{uu}(\alpha, \beta, \tau) \rangle = R_{uu}(\alpha, \beta, \tau)$$

Fortunately it has been found that the estimated correlations may be modified by some even function of τ . While these modified estimated correlation functions may not be good estimates of the true correlation, their Fourier transforms can be very respectable estimates of "smoothed" values of the true spectrum!

The modified estimated correlation function may be written

$$\tilde{R}_{uu}(\alpha, \beta, \tau) = D(\tau) \hat{R}_{uu}(\alpha, \beta, \tau) \quad (\text{a19})$$

where $D(\tau)$ may be regarded as a window of variable transmission which modifies the values of $\hat{R}_{uu}(\alpha, \beta, \tau)$ for different lags, and

$$D(0) = 1$$

$$D(\tau) = 0 \quad \text{for } |\tau| > \tau_{\max}$$

1. $\langle \rangle$ indicates an ensemble average.

Even though $\hat{R}_{uu}(\alpha, \beta, \tau)$ was not defined for $|\tau| > \tau_{\max}$, $\tilde{R}_{uu}(\alpha, \beta, \tau)$ is and so has a definite Fourier transform $\phi_{uu}(\alpha, \beta, f)$ which satisfies the convolution integral

$$\begin{aligned}\tilde{\phi}_{uu}(\alpha, \beta, f) &= \int_{-\infty}^{\infty} D(\tau) \hat{R}_{uu}(\alpha, \beta, \tau) e^{-i2\pi f\tau} d\tau \\ &= \int_{-\infty}^{\infty} D(\tau) \left[\int_{-\infty}^{\infty} \phi_{uu}(\alpha, \beta, f') e^{i2\pi f'\tau} df' \right] e^{-i2\pi f\tau} d\tau\end{aligned}$$

i.e.,

$$\tilde{\phi}_{uu}(\alpha, \beta, f) = \int_{-\infty}^{\infty} Q(f-f') \hat{\phi}_{uu}(\alpha, \beta, f') df' \quad (a21)$$

Even though $\hat{\phi}_{uu}(\alpha, \beta, f')$ is not determinate since $\hat{R}_{uu}(\alpha, \beta, \tau)$ is not specified for $|\tau| > \tau_{\max}$, we have

$$\langle \tilde{R}_{uu}(\alpha, \beta, \tau) \rangle = D(\tau) R_{uu}(\alpha, \beta, \tau) \quad (a22)$$

$$\text{so} \quad \langle \phi_{uu}(\alpha, \beta, f) \rangle = \int_{-\infty}^{\infty} Q(f-f') \phi_{uu}(\alpha, \beta, f') df \quad (a23) \underline{A}.$$

It can be seen that $\langle \tilde{\phi}_{uu}(\alpha, \beta, f) \rangle$ is an average over frequency of the true power spectral density $\phi_{uu}(\alpha, \beta, f')$ over frequencies near f' .

In general one would like to concentrate the main lobe of $Q(f)$ near $f = 0$, which requires a flat blocky window. At the same time the lag window must be smooth and gentle changing to reduce side lobes and go to zero for $|\tau| \geq \tau_{\max}$, so a compromise is necessary.

One simple and convenient window which has been found to work satisfactorily is the "Hanning" window, (see Fig.65).

$$\begin{aligned}D(\tau) &= \frac{1}{2} \left[1 + \cos \frac{\pi\tau}{\tau_{\max}} \right] \text{ for } |\tau| < \tau_{\max} \\ &= 0 \quad \text{for } |\tau| \geq \tau_{\max}\end{aligned}$$

For the case of data uniformly spaced in time (as in this experiment), it is most expedient to first transform and then convolve (by equation (a21))

$$\int_{-\infty}^{\infty} D(\tau) e^{-i2\pi f\tau} d\tau = Q(f)$$

i.e.,

$$Q(f) = \int_{-\infty}^{\infty} \left(\frac{1}{2} + \frac{1}{2} \cos \frac{\pi \tau}{\tau_{\max}} \right) e^{-i2\pi f \tau} d\tau$$

$$= \frac{1}{2} \delta(f) + \frac{1}{4} \left[\delta(f+f') + \delta(f-f') \right] \quad (a23)_B.$$

where $f' = 1/2\tau_{\max}$

Thus

$$\tilde{\phi}_{uu}(\alpha, \beta, f) = \int_{-\infty}^{\infty} \left\{ \frac{1}{2} \delta(f-\lambda) + \frac{1}{4} [\delta(f+f'-\lambda) + \delta(f-f'-\lambda)] \right\} \hat{\phi}_{uu}(\alpha, \beta, \lambda) d\lambda \quad (a24)$$

Now $1/2\tau_{\max} = f' = \Delta f$ represents the spacing of the frequency estimates, i.e.,

$$\tilde{\phi}_{uu}(\alpha, \beta, f) = \frac{1}{2} \hat{\phi}_{uu}(f) + \frac{1}{4} \left[\hat{\phi}_{uu}(f + \Delta f) + \hat{\phi}_{uu}(f - \Delta f) \right] \quad (a25)$$

The application of (a 25) is very simple, and for a single sided spectrum (double sided spectra were considered above) consists of smoothing in the following manner.

$$\tilde{\phi}_{uu}(f = 0) = .5 \hat{\phi}_{uu}(f = 0) + .5 \hat{\phi}_{uu}(\Delta f)$$

$$\tilde{\phi}_{uu}(f) = .25 \hat{\phi}_{uu}(f - \Delta f) + .5 \hat{\phi}_{uu}(f) + .25 \hat{\phi}_{uu}(f + \Delta f) \quad (a26)$$

$$\tilde{\phi}_{uu}(f = f_{\max}) = .5 \phi_{uu}(f_{\max}) + .5 \phi_{uu}(f_{\max} - \Delta f)$$

Finally, in order that our modified spectral estimates exhibit as much independence as possible, only every second frequency point is retained after application of the Hanning window.

3. SCALE OF TURBULENCE AND WAVE LENGTH

The lengths L_x and L_z defined by

$$L_x(z) = \bar{U}(z) \int_0^{\infty} \frac{\tilde{R}_{uu}(\alpha, \alpha, \tau)}{\tilde{R}_{uu}(\alpha, \alpha, 0)} dx \quad (a27)$$

$$L_z(z) = \int_0^{\infty} \frac{\tilde{R}_{uu}(\alpha, \beta, \tau)}{\tilde{R}_{uu}(\alpha, \alpha, 0)} dz \quad (a28)$$

are called the longitudinal and lateral scales respectively. They are convenient

measures of the linear extent of the region within which velocities are appreciably correlated. In the particular case of shear turbulent flow these scales vary with lateral position, and hence the notation $L(z)$ where z is lateral (vertical) position.

When the ratios $\frac{\tilde{R}_{uu}(\alpha, \beta, 0)}{\tilde{R}_{uu}(\alpha, \alpha, 0)}$ are plotted versus $\alpha - \beta$, for the lateral

scale it is found that the resultant curve depends on whether β is taken upwards or downwards from the fixed probe position. This can be seen in Fig. 47. The quoted scale values are averages of the two separate scales.

The significant turbulence wave lengths for excitation of normal modes are defined by

$$\lambda_n = \bar{U}/f_n \quad (a.29)$$

where f_n is the frequency of the n th mode of vibration of the cylinder. As long as $\lambda_n \gg b$, it is reasonable to assume that the pressure distribution over the cylinder is two dimensional. Table 2 shows λ_1, λ_2 and λ_3 and suggests that the assumption of two-dimensionality is reasonable, for the first modes and borderline for the second.

From the form of the narrow band correlation (reference 16) Fig. 40 one would expect that failure of the theory would occur for frequencies where λ approaches the lateral dimension of the structure. In such a case, you would not have correlated flow over the cylinder, and the two-dimensional assumptions would be suspect.

APPENDIX B: STRUCTURE RESPONSE

The following is a summary of the "Theory of the Response of a Slender Structure to a Turbulent Wind with Shear", by B. Etkin. For the complete analysis see reference 7.

1. PRELIMINARIES

The situation is shown in Fig.60, $\bar{U}(z)$ is the mean wind profile (see Fig.2) and $u(x,t)$ is the fluctuating component (see Fig.3) in the direction of the mean wind (drag direction). $\bar{X}(z)$ is the mean deflection of the structure associated with $\bar{U}(z)$, and $x(z,t)$ is the vibrational motion associated with $u(z,t)$. The local running load on the structure is $W(z,t)$ of which $\bar{W}(z)$ is the mean and $w(z,t)$ the fluctuating part. Thus

$$U(z,t) = \bar{U}(z) + u(z,t) \quad (b.1)$$

$$W(z,t) = \bar{W}(z) + w(z,t) \quad (b.2)$$

$$X(z,t) = \bar{X}(z) + x(z,t) \quad (b.3)$$

and the relative wind is

$$U'(z,t) = U(z,t) - \dot{y}(z,t) \quad (b.4)$$

Assuming the local load $W(z,t)$ per unit length is given by "strip theory" as

$$W(z,t) = \ell_1(z) U'^2(z,t) + \ell_2(z) \dot{U}'^2(z,t) \quad (b.5)$$

where

$$\ell_1(z) = C_D(z) b(z) \rho / 2 \quad (b.6)$$

and

$$\ell_2(z) = k(z) b^2(z) \rho \quad (b.7)$$

Equations (b.5) to (b.7), as used subsequently, imply that k and C_D are independent of the turbulence. This assumption requires that the lateral dimension is small compared to the wave length, λ , of the turbulence defined as

$$\lambda = \bar{U} / f \quad (\text{see A3}) \quad (b.8)$$

2. FLUCTUATING LOAD

From (b.5), (b.6), (b.7) and (b.8) we have

$$W(z,t) = \ell_1(z) [U^2 - 2 U \dot{x} + \dot{x}^2] + \ell_2(z) [\dot{U} - \dot{x}]^2 \quad (b.9)$$

Writing the fluctuating load as

$$w(z,t) = W(z,t) - \bar{W}(z) \quad (b.10)$$

where

$$\bar{W}(z) = \ell_1(z) [\bar{U}^2 - 2\bar{U}\bar{x} + \bar{x}^2] \quad (b.11)$$

we get

$$w(z,t) = \ell_1(z) [U^2 - \bar{U}^2 - 2U\bar{x} + 2\bar{U}\bar{x} + \dot{x}^2 - \bar{\dot{x}}^2] + \ell_2(z) [\dot{U} - \dot{\bar{x}}] \quad (b.12)$$

By assuming that the turbulence and structure motion are small enough that second order terms may be neglected, and then removing terms which do not depend on the turbulence we obtain the load associated with the turbulence

$$w'(z,t) = 2\ell_1(z)\bar{U}(z)u(z,t) + \ell_2(z)\dot{u}(z,t) \quad (b.13)$$

3. MODAL REPRESENTATION

Let the displacement of the structure be expanded in the normal modes of vibration, not in a vacuum, but in the presence of the steady non-uniform $\bar{U}(z)$. Thus the turbulence terms u and \dot{u} are absent from the associated autonomous equations of motion. The displacement from the mean position is then

$$x(z,t) = \sum_{n=1}^{\infty} F_n(z) q_n(t) \quad (b.14)$$

where $F_n(z)$ are the mode shapes and the $q_n(t)$ are generalized co-ordinates. The equations of motion in the absence of turbulence are then

$$\ddot{q}_n + 2\zeta_{Tn}\omega_n\dot{q}_n + \omega_n^2 q_n = 0 \quad (b.15)$$

When turbulence is present, the non autonomous system of equations is

$$\ddot{q}_n + 2\zeta_{Tn}\omega_n\dot{q}_n + \omega_n^2 q_n = \mathcal{F}_n(t)/I_n \quad (b.16)$$

where \mathcal{F}_n is the generalized force associated with the turbulent input and I_n is the generalized inertia in the n th mode.

$$I_n = \int_0^l F_n^2(z) m'(z) dz \quad (b.17)$$

\mathcal{F}_n is calculated from the work done, δW , during a virtual displacement δq_n , and is

$$\begin{aligned} \mathcal{F}_n(t) = & \int_0^l g_n(z) u(z,t) dz \\ & + \int_0^l h_n(z) \dot{u}(z,t) dz \end{aligned} \quad (b.18)$$

where

$$g_n(z) = 2 \bar{U}(z) \ell_1(z) F_n(z) \quad (b.19)$$

$$h_n(z) = \ell_2(z) F_n(z) \quad (b.20)$$

Figure 62 shows the manner in which the individual modes are excited and contribute to the total deflection x .

4. SPECTRAL ANALYSIS

The spectral density of x is given by the fundamental equation

$$\phi_{xx}(z, f) = \sum_m \sum_n F_m(z) F_n(z) G_m^*(if) G_n(if) \phi_{\mathcal{F}_m \mathcal{F}_n}(f) \quad (b.21)$$

$\phi_{\mathcal{F}_m \mathcal{F}_n}(f)$ is the cross spectral density of $\mathcal{F}_m(t)$ and $\mathcal{F}_n(t)$, while $G_n(if)$ is the transfer function relating $x(z, t)$ to $\mathcal{F}_n(t)$.

From the equations of motion

$$G_n(if) = [I_n(4\pi^2 f_n^2 - 4\pi^2 f^2 + 8i\pi^2 \zeta_n f f_n)]^{-1} \quad (b.22)$$

The spectrum function $\phi_{\mathcal{F}_m \mathcal{F}_n}(f)$ is the basic information needed to assess the behaviour of the structure.

To obtain the general spectrum functions for the driving forces in terms of the turbulence velocity spectra, we proceed via the correlation function.

$$\phi_{\mathcal{F}_m \mathcal{F}_n}(f) = \int_{-\infty}^{\infty} R_{mn}(\tau) e^{-i2\pi f \tau} d\tau \quad (b.23)$$

where

$$R_{mn}(\tau) = \langle \mathcal{F}_m(t) \mathcal{F}_n(t + \tau) \rangle \quad (b.24)$$

and $\langle \rangle$ represents an ensemble average which is equivalent to a time average for this case.

On forming the appropriate products of the \mathcal{F} 's (given by equation (b.18)) as shown by equation (b.24) and noting;

- (i) that the order of integration and averaging can be interchanged
- (ii) that the mean products in these integrals are themselves cross correlations
- (iii) that

$$\phi_{\dot{u}\dot{u}} = \omega^2 \phi_{uu}$$

$$\phi_{\dot{u}u} = -i\omega \phi_{uu}$$

$$\phi_{\dot{u}\dot{u}} = i\omega \phi_{uu}$$

we obtain the cross correlation of \mathcal{F}_m and \mathcal{F}_n , which in turn can be Fourier transformed to give the required spectrum. The resultant generalized force spectrum is

$$\begin{aligned} \phi_{\mathcal{F}_m \mathcal{F}_n}(f) = & \int_0^{\ell} \int_0^{\ell} \phi_{uu}(\alpha, \beta, f) \left\{ g_n(\alpha) g_m(\beta) + 4\pi^2 f^2 h_n(\alpha) h_m(\beta) \right. \\ & \left. + i 2\pi f [g_n(\alpha) h_m(\beta) - g_m(\beta) h_n(\alpha)] \right\} d\alpha d\beta \quad (b.25) \end{aligned}$$

Obviously the only spectrum function needed to evaluate all the terms is $\phi_{uu}(\alpha, \beta, f)$, the velocity cross spectrum.

APPENDIX C: SYSTEM PARAMETERS

1. GENERAL

m = mass/unit length = 2.080×10^{-3} slugs/ft.

k = 2-D added mass coefficient = $\pi/4$

C_D = 1.2

l = total cylinder length = 29.5 inches

l' = exposed cylinder length = 27.0 inches

b = cylinder diameter = .50 inches

ρ = 2.38×10^{-3} slugs/ft.

EI = bending stiffness = 5180.0 lb.inch²

$m = m + kb^2\rho = 2.083 \times 10^{-3}$ slugs/ft.

2. MODE FREQUENCIES AND SHAPES

The differential equation for a free slender beam undergoing small vibration is

$$(EI x'')'' + m\ddot{x} = 0 \quad (c.1)$$

where $x = x(z,t)$ is the lateral deflection. By applying boundary conditions applicable to a cantilever, it can be shown (reference 8) that the natural mode frequencies are given by (see table 1)

$$f_n = \frac{a_n^2}{2} \frac{\pi}{l^2} \left[\frac{EI}{m} \right]^{\frac{1}{2}} \quad (c.2)$$

where $a_1 = .597$, $a_2 = 1.49$, $a_3 = 5/2$, $a_4 = 7/2$ -----

The natural mode shapes are given by (see Fig.63),

$$F_n(z) = \left[\frac{\sin p l - \sinh p l}{\cosh p l + \cos p l} \right] (\sinh p z - \sin p z) \\ + (\cosh p z - \cos p z) \quad (c.3)$$

where

$$p = \left[\frac{4 \pi^2 f_n^2 m'}{EI} \right]^{\frac{1}{4}}$$

The second derivative of the mode shape function evaluated at $z = 0$ is

$$\left. \frac{d^2 F_n}{dz^2} \right|_{z=0} = F_n''(0) = 2 \left[\frac{2\pi f_n^2 m'}{EI} \right]^{\frac{1}{2}} \quad (c.4)$$

3. GENERALIZED INERTIA

The expression for the generalized inertia is given by equation (b.17) (see table 1).

$$I_n = \int_0^l F_n^2(z) m'(z) dz$$

i.e.,

$$I_n = m' \int_0^l F_n^2(z) dz \quad (c.5)$$

for m' constant.

4. DAMPING

(a) Structural:

The structural damping was measured for the first 3 modes by recording the decay with time of the signal from the cylinder strain gauges on visicorder tape after the signal was passed through a narrow filter centered about the natural frequency in question. An exponential decay scheme representative of a second order system was assumed. i.e.,

$$e(t) = e_0 e^{-\zeta_{s_n}^2 2\pi f_n t} \quad (c.6)$$

where e_0 was the initial signal and ζ_{s_n} is the structural damping ratio.

From (c.6)

$$\ln(e/e_0) = -\zeta_{s_n}^2 2\pi f_n t$$

thus (see table 1)

$$\zeta_{s_n} = (-1/2\pi f_n t) \ln(e/e_0) \quad (c.7)$$

The variation of damping with initial displacement was also investigated and the results are shown in Fig.64.

(b) Aerodynamic:

The aerodynamic damping coefficient per unit length is given by

$$c_a(z) = 2 \ell_1 \bar{U} \cdot (z) F_n(z)^2 \quad (c.8)$$

Thus the damping ratio for the total model length may be expressed as (see table 1)

$$\zeta_{a_n} = \frac{l_1}{I_n \omega_n} \int_0^{l'} F_n(z)^2 \bar{U}(z) dz \quad (c.9)$$

(c) Total:

The total damping is given by (see table 1)

$$\zeta_{T_n} = \zeta_{a_n} + \zeta_{s_n}$$

5. TRANSFER FUNCTION

The transfer function for the second order system is (from (b.22))

$$G_n(if) = \left\{ I_n \left[(2\pi f_n)^2 - (2\pi f)^2 + i 8\pi^2 f f_n \zeta_{T_n} \right] \right\}^{-1}$$

and so

$$|G_n(if)|^2 = \left\{ I_n^2 \left[(4\pi^2 f_n^2 - 4\pi^2 f^2) + 64\pi^4 f^2 \zeta_{T_n}^2 f_n^2 \right] \right\}^{-1}$$

Equation (c.11) is shown in Fig.66.

APPENDIX D: ERRATA FOR PREVIOUS CAMPBELL * ETKIN REPORT

1. Appendix A: Equation (21), p.A6 should read

$$\phi_{MM}(\omega) = \frac{1}{2\pi} \int_{-\infty}^{\infty} R_{mm}(\tau) e^{-i\omega\tau} d\tau$$

Equations (30, p.A8 should read

$$\phi_1 = \frac{1}{2\pi} \int_{-\infty}^{\infty} R_1 \cos \omega\tau d\tau$$

$$\phi_2 = \frac{1}{2\pi} \int_{-\infty}^{\infty} R_2 \sin \omega\tau d\tau$$

2. Figure 10: The ordinate designation should read

$$\frac{2 \phi_{MM}(\omega)}{10}$$

n	f_n (cps)	$F_n''(0)$ (in^{-2})	I_n (slug/12)	ζ_{s_n}	ζ_{a_n}	ζ_{t_n}
1	12.2	8.090×10^{-3}	4.387×10^{-4}	2.30×10^{-3}	1.61×10^{-2}	1.84×10^{-2}
2	76.0	5.040×10^{-2}	4.379×10^{-4}	3.75×10^{-3}	2.01×10^{-3}	5.76×10^{-3}
3	213.8	1.419×10^{-1}	4.403×10^{-4}	5.63×10^{-3}	6.57×10^{-4}	6.29×10^{-3}

TABLE 1.

z	\bar{U}	λ_1	λ_2	λ_3
.125	7.54	7.40	1.20	.43
2.70	12.8	12.6	2.03	.72
5.40	16.9	16.6	2.68	.95
8.10	22.0	21.7	3.49	1.24
10.8	26.6	26.2	4.07	1.50
13.5	31.3	30.7	4.93	1.75

z	\bar{U}	λ_1	λ_2	λ_3
16.2	35.5	35.0	5.63	2.00
18.9	40.2	39.7	6.38	2.37
21.6	44.3	43.7	7.03	2.50
24.3	48.3	47.6	7.56	2.73
27.0	51.5	50.8	8.18	2.91

TABLE 2.

f	$(\Delta\sigma_D^2)_{UF}^T$	$(\Delta\sigma_D^2)_F^T$	$(\Delta\sigma_D^2)_{exp}^T$	$\Delta\sigma_F^2/\Delta\sigma_{exp}^2$
2-11	$.837 \times 10^0$	$.882 \times 10^0$	1.096×10^0	.806
11-14	5.19×10^0	5.38×10^0	4.67×10^0	1.15
14-20	1.26×10^{-1}	1.34×10^{-1}	1.60×10^{-1}	.840
20-70	7.80×10^{-3}	1.23×10^{-2}	1.40×10^{-2}	.880
70-80	1.38×10^{-2}	1.52×10^{-2}	$.715 \times 10^{-2}$	2.13
80-100	2.24×10^{-3}	7.08×10^{-3}	3.49×10^{-2}	.203
Total	6.18	6.43	5.99	1.07

TABLE 3.

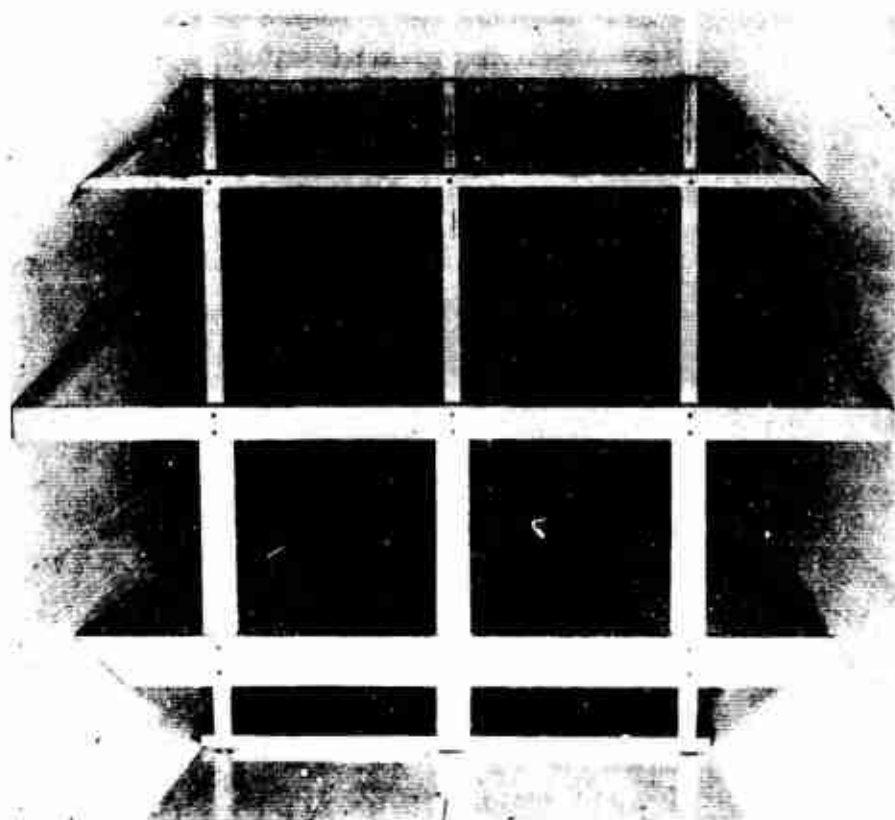


Fig.1 - SHEAR GRID

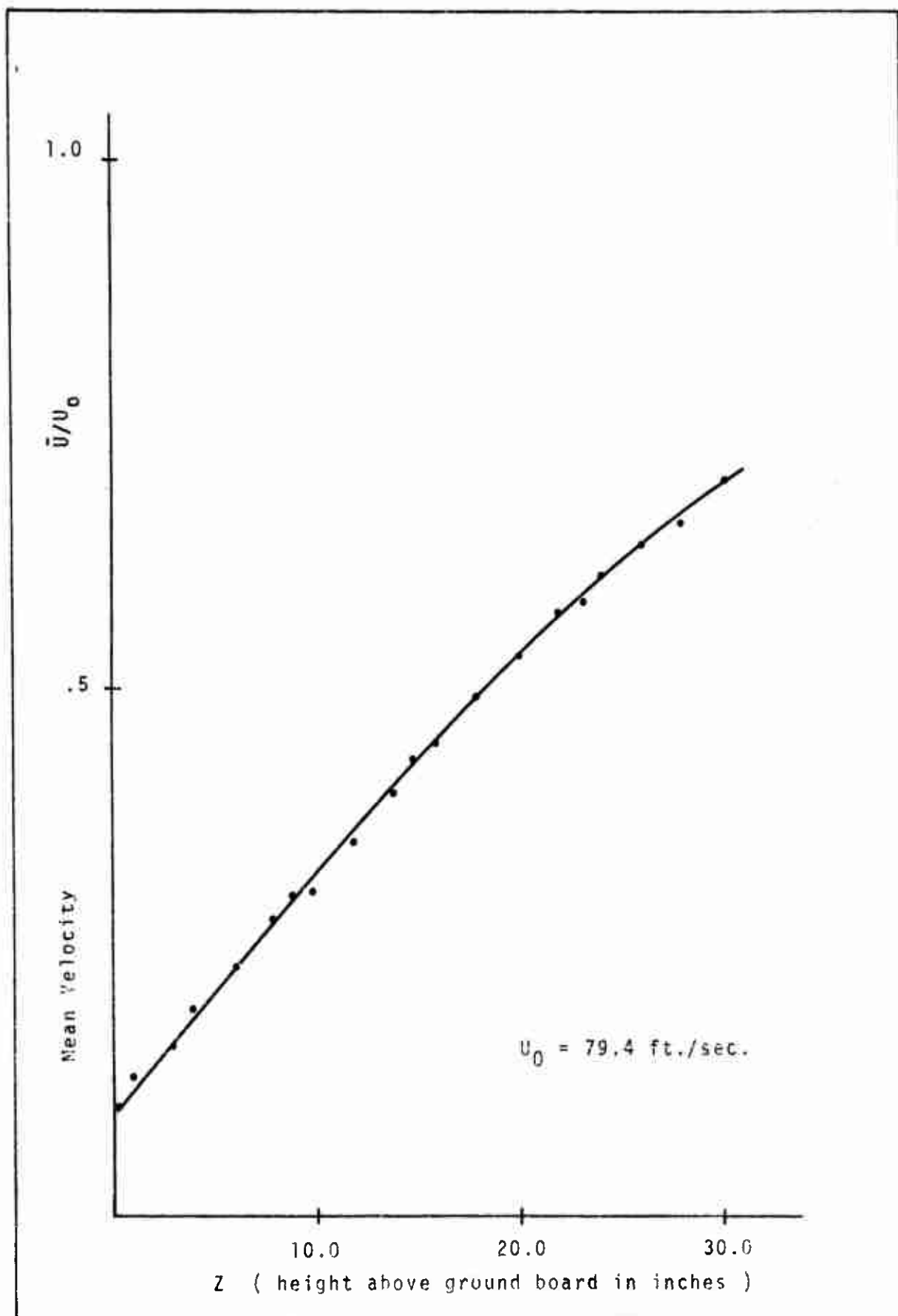


Fig.2 - MEAN VELOCITY PROFILE

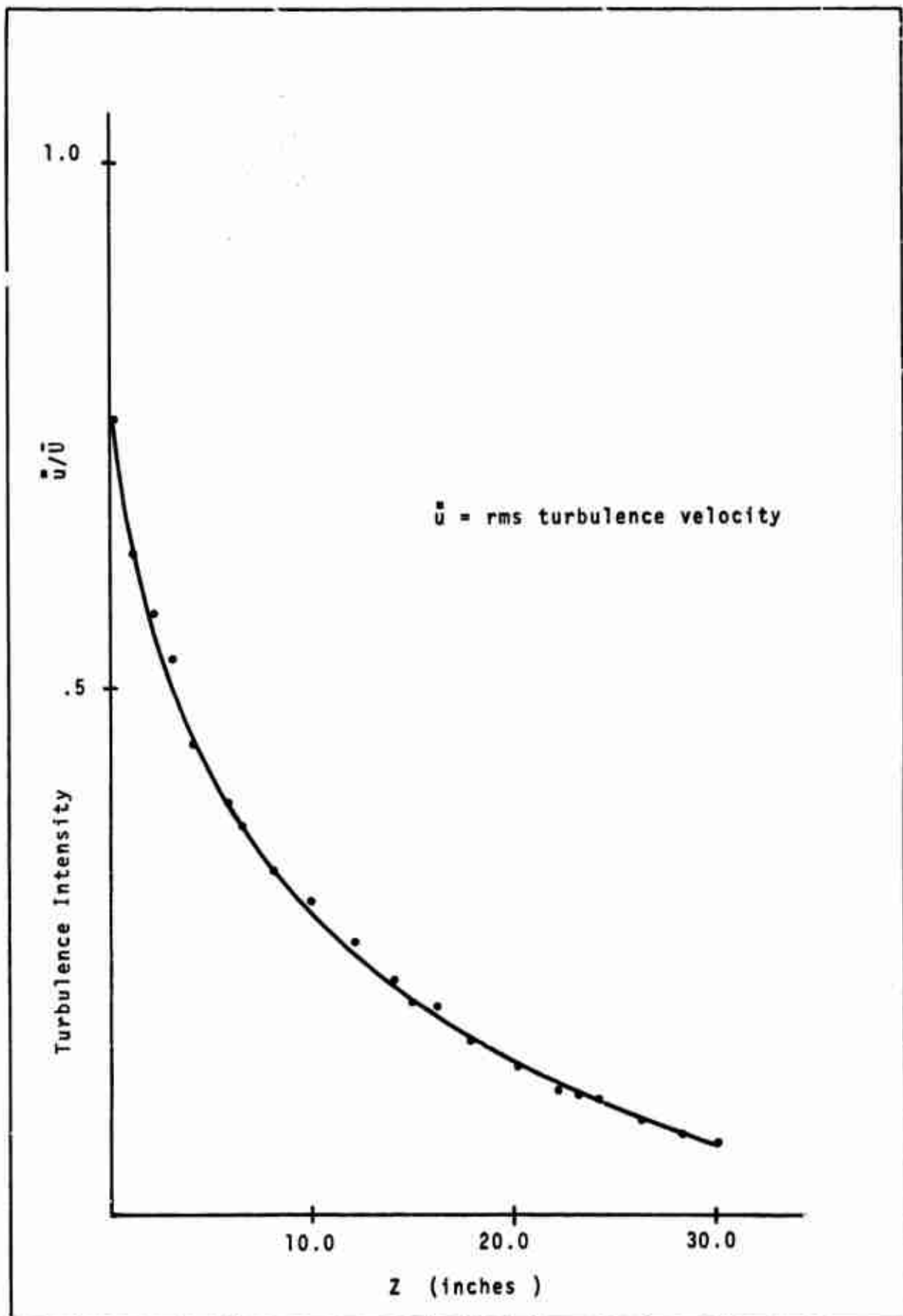
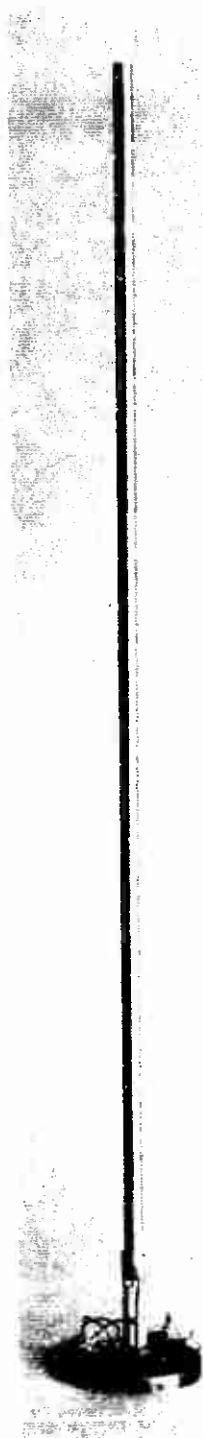


Fig.3 - TURBULENCE INTENSITY SURVEY



Campbell's model



Modified model

Fig.4 - GENERAL VIEW OF MODEL

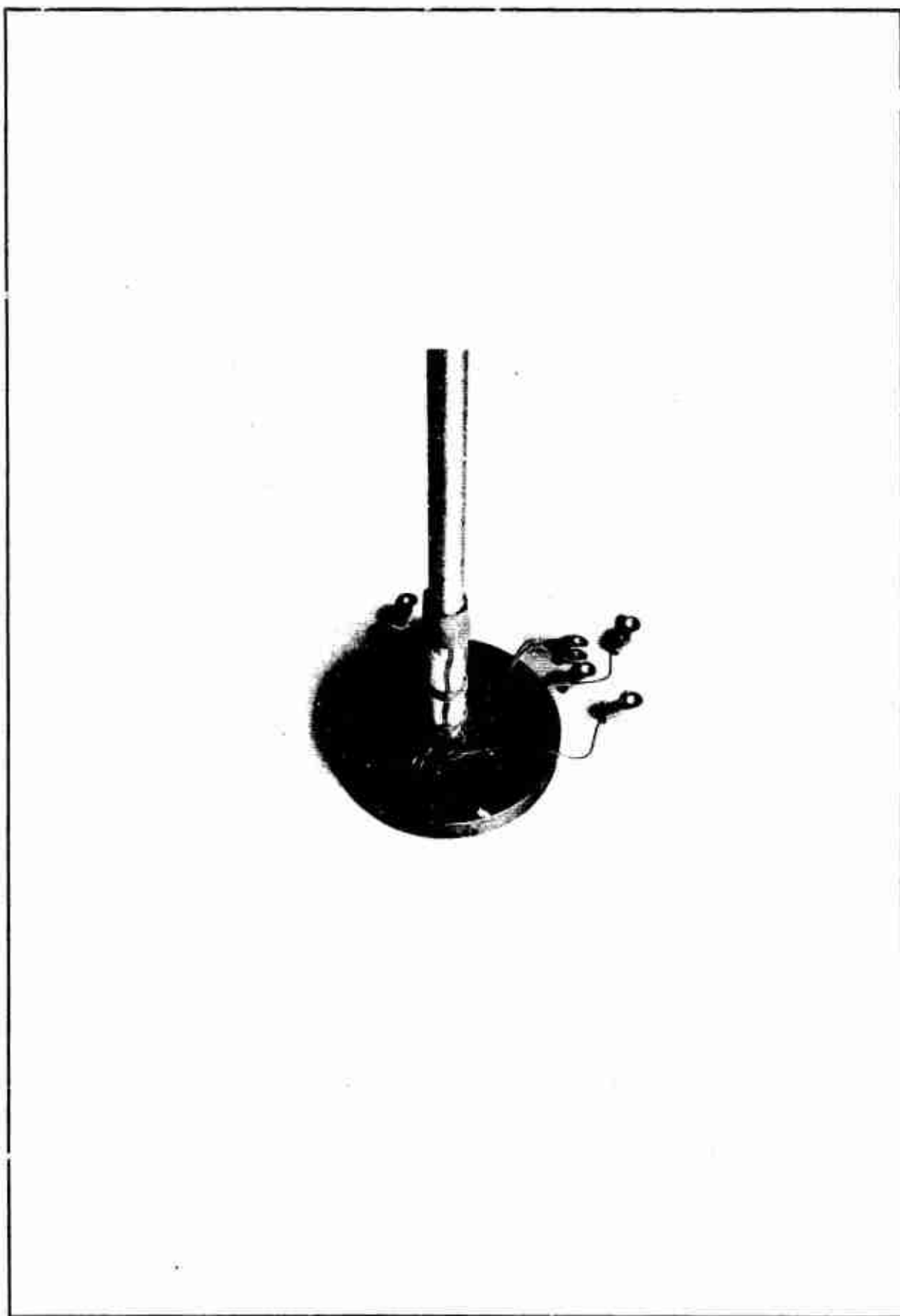


Fig.5 - STRAIN GAUGES MOUNTED ON MODEL

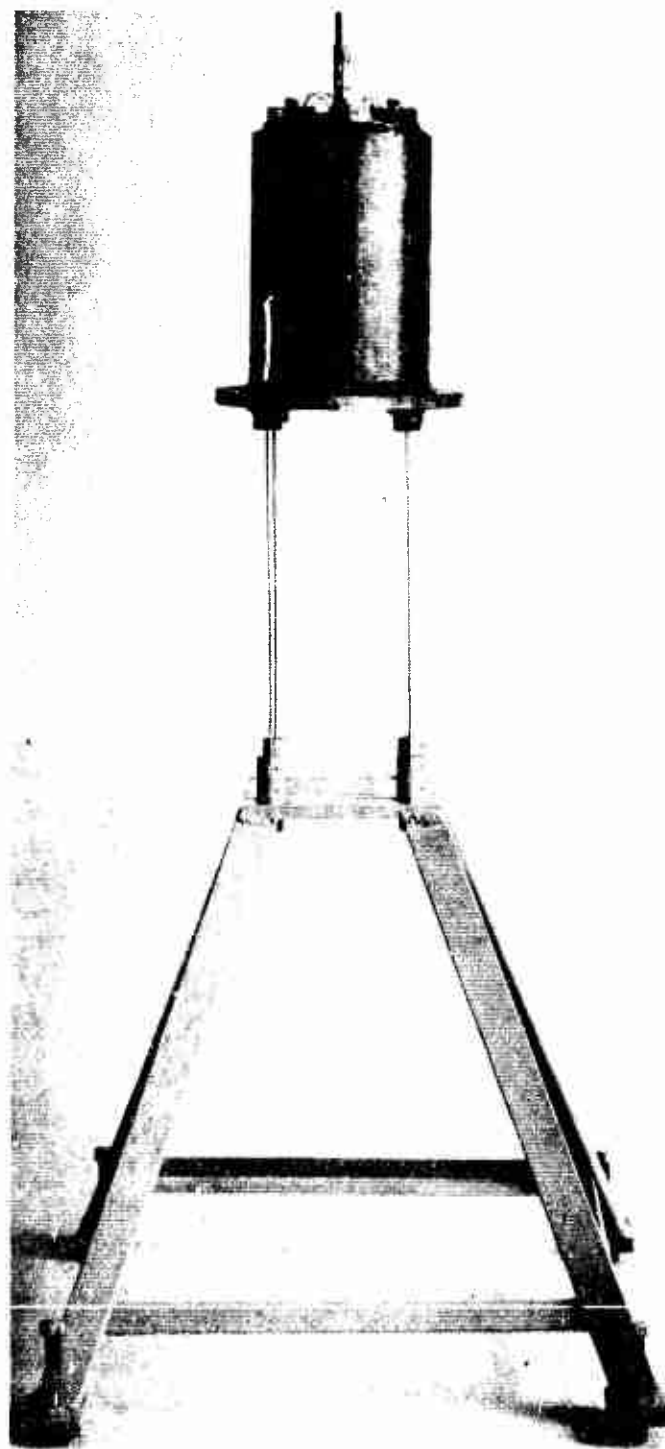


Fig.6 - MODEL MOUNTING STRUCTURE

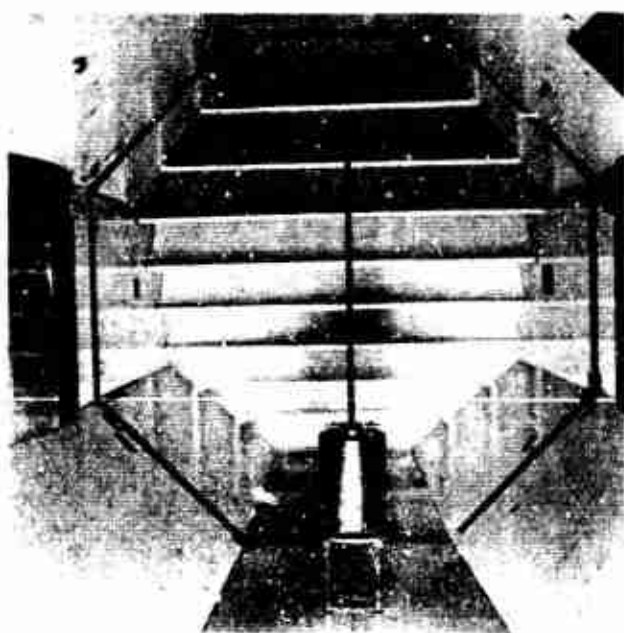
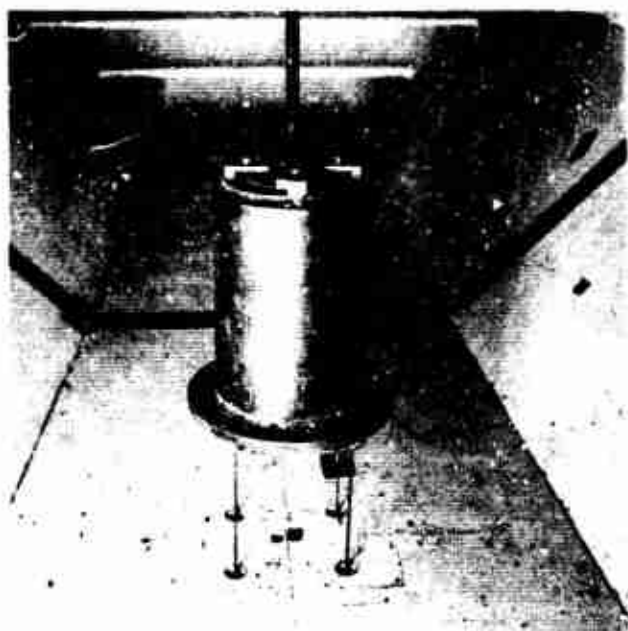


Fig.7 - MOUNT INSTALLATION DETAIL

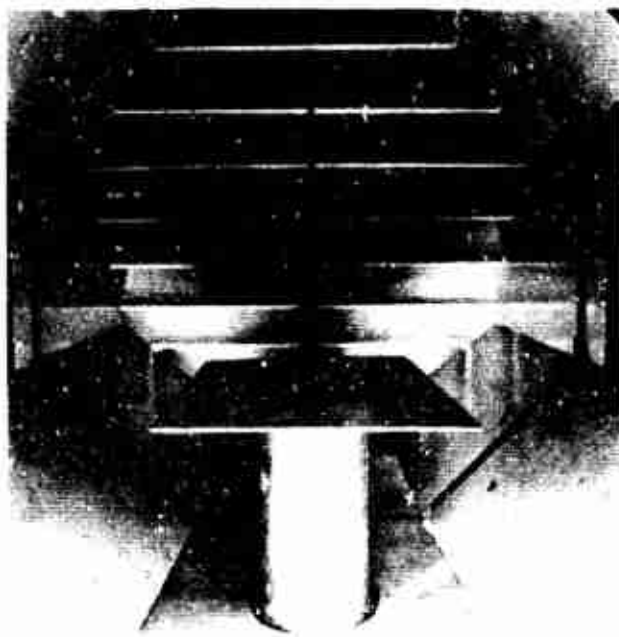
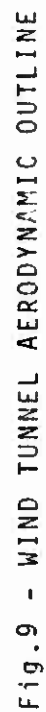
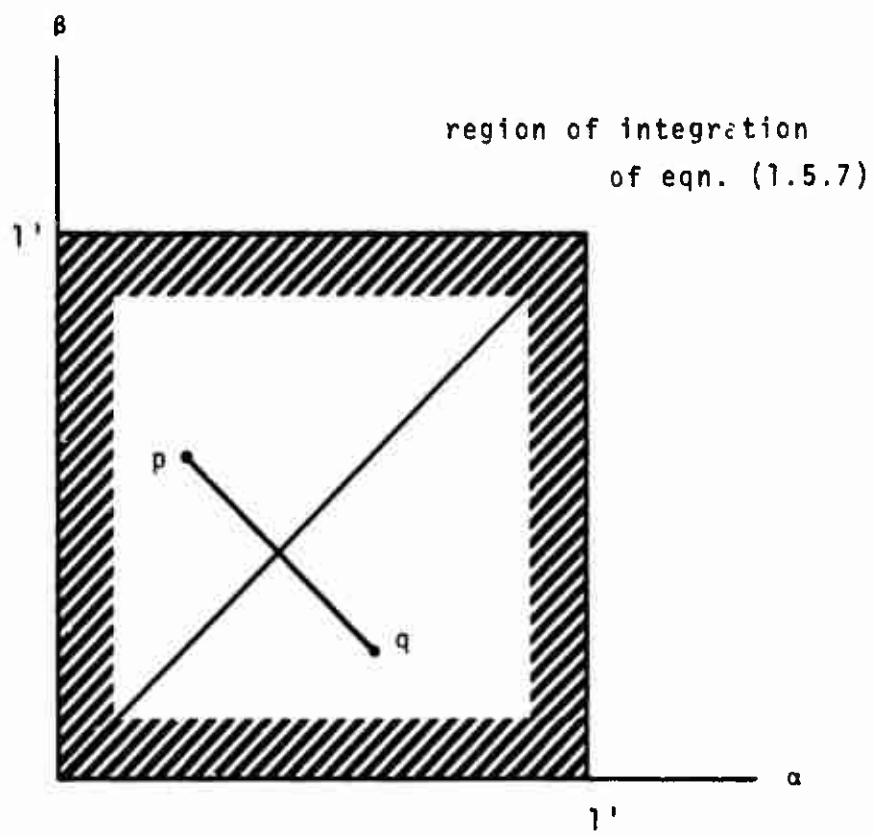


Fig.8 - COMPLETE MODEL INSTALLATION





$l' = \text{exposed cylinder length}$

Fig.10 - (α, β) DOMAIN

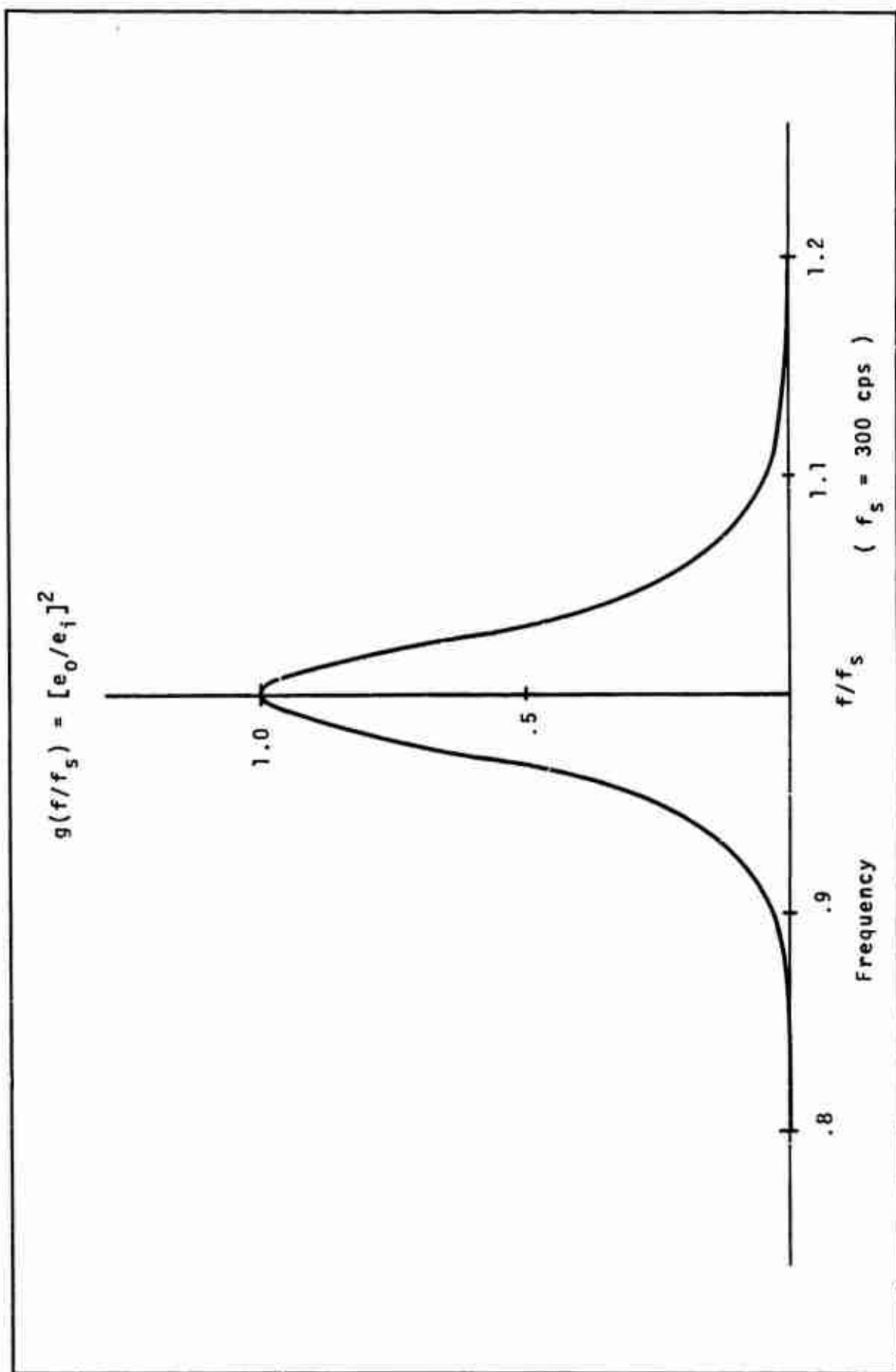


Fig.11 - ANALYSER FILTER BAND-SHAPE

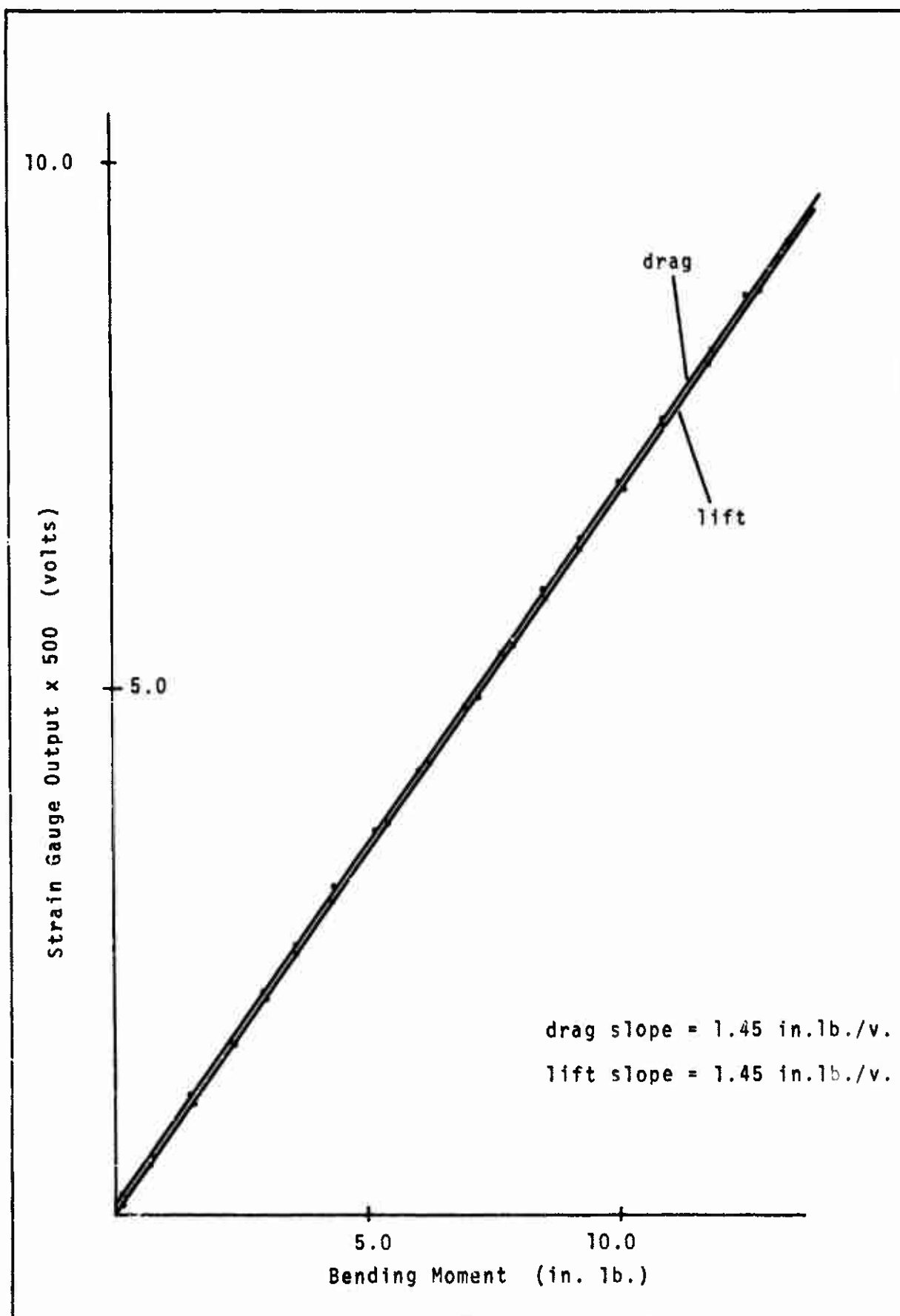


Fig.12 - STRAIN GAUGE CALIBRATION

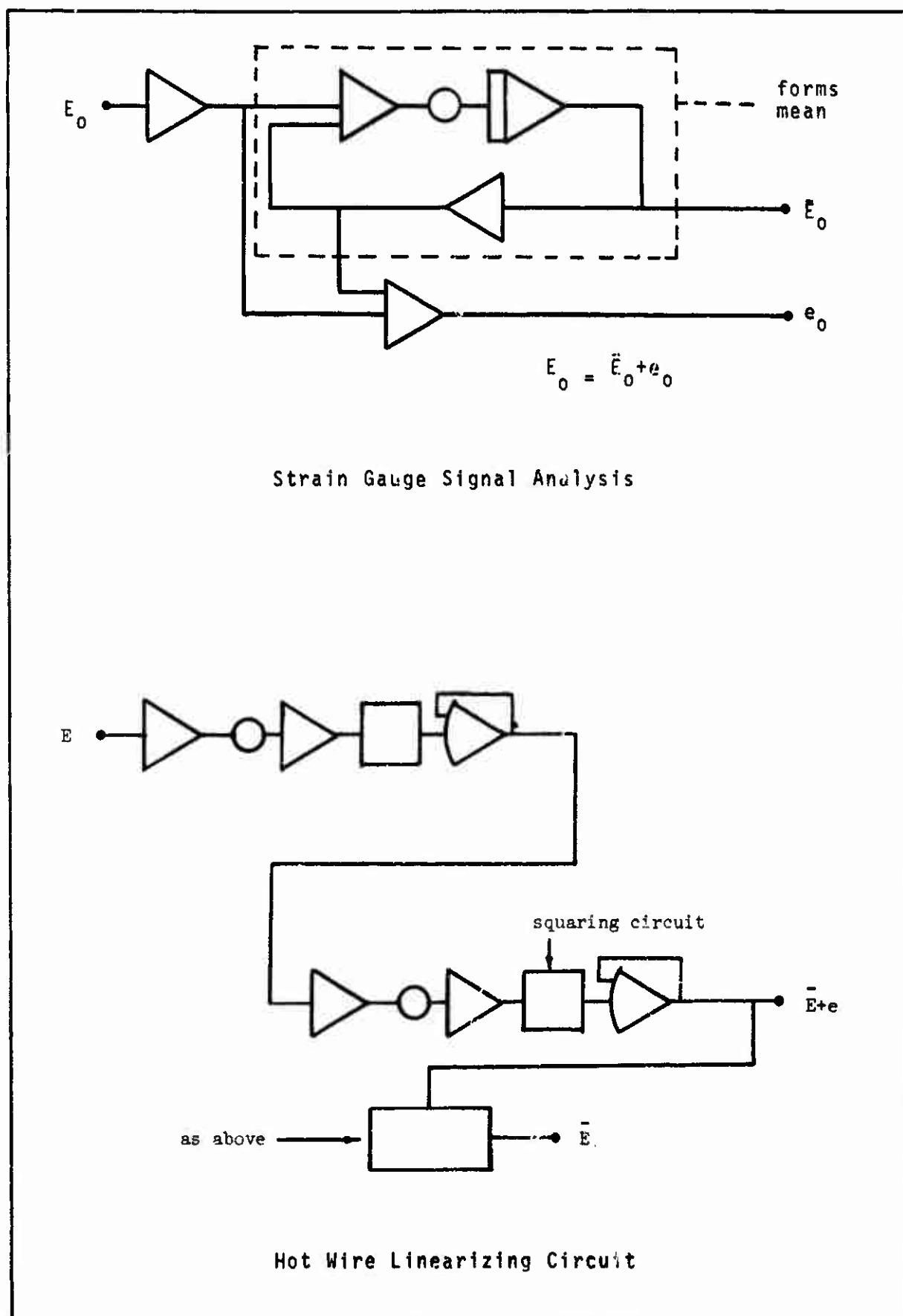


Fig.13 - ANALOGUE ANALYSIS CIRCUITRY

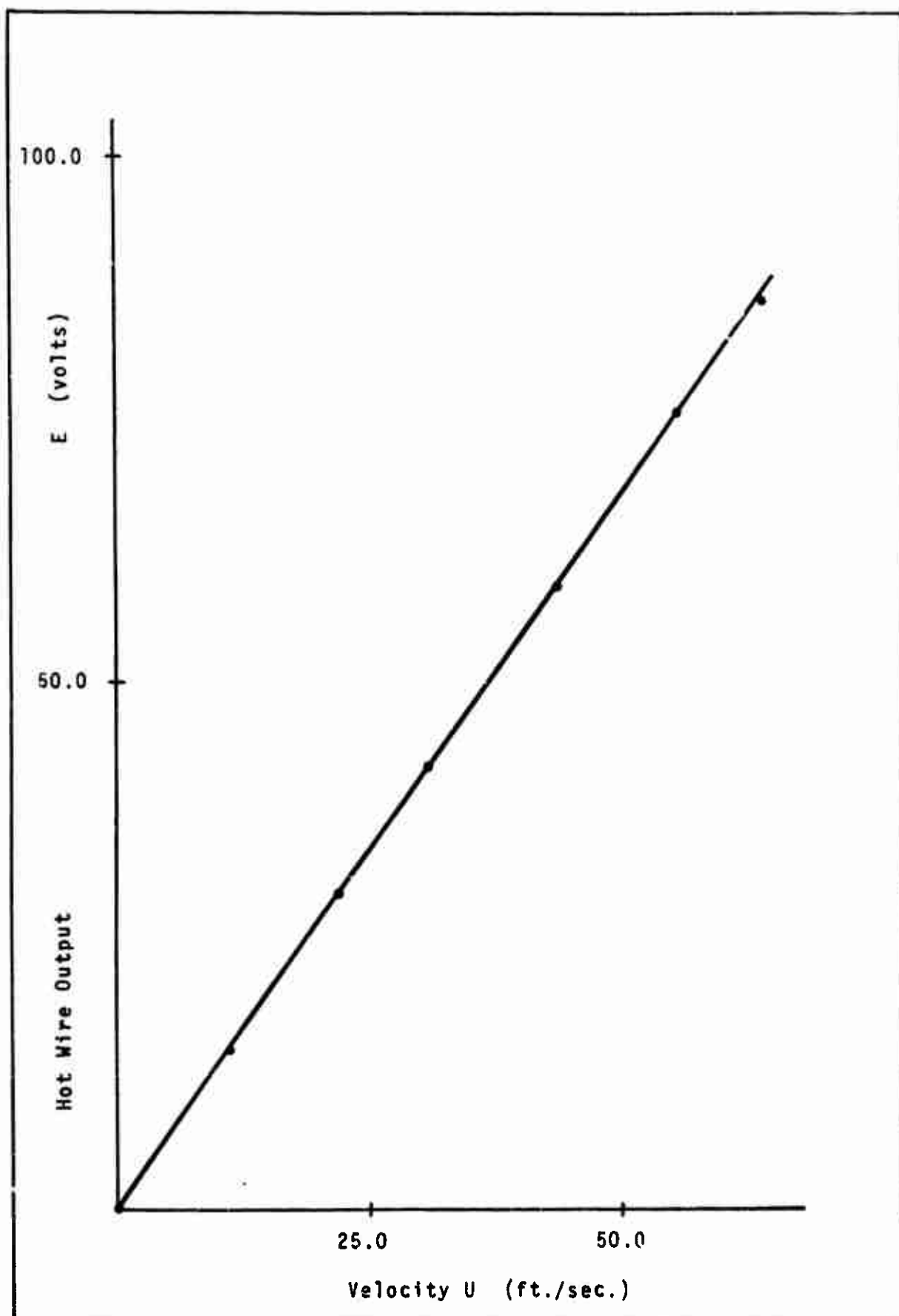
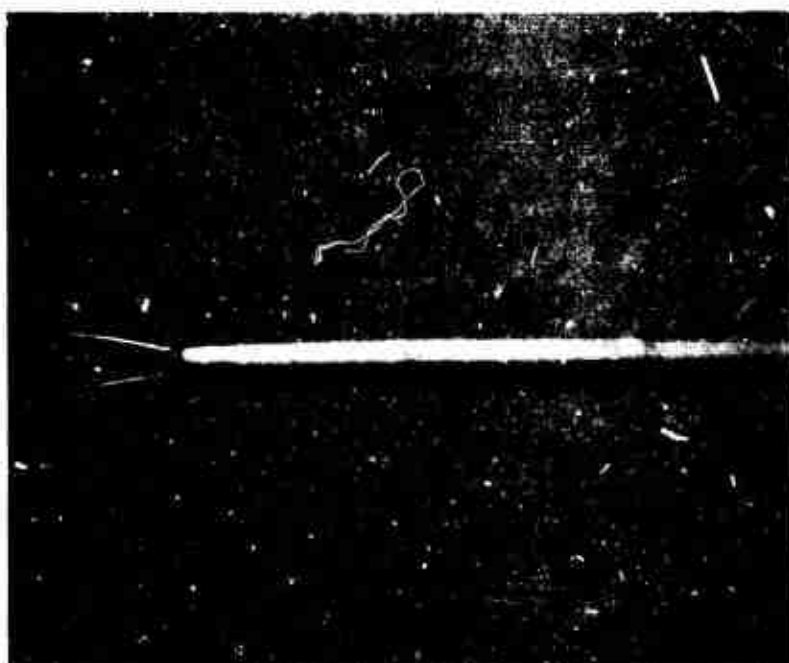
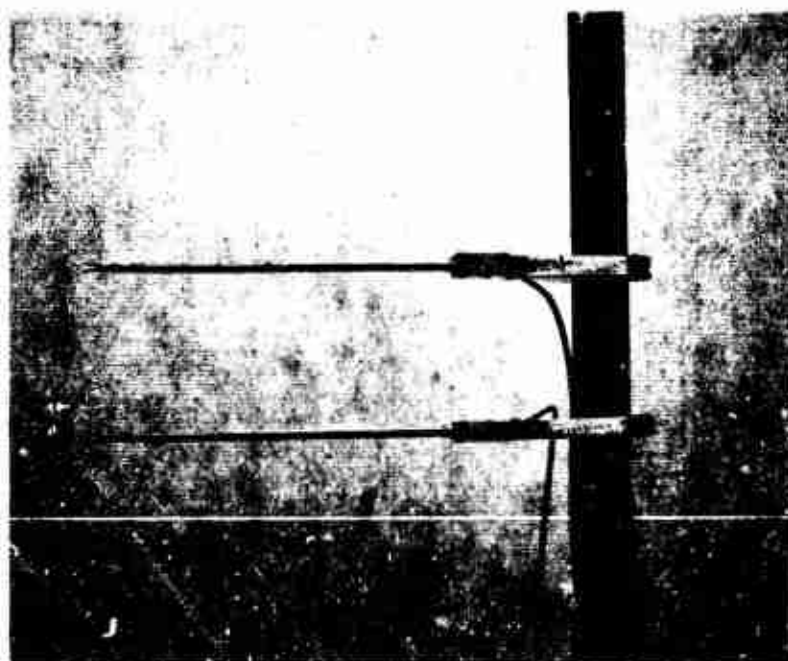


Fig.14 - HOT WIRE CALIBRATION

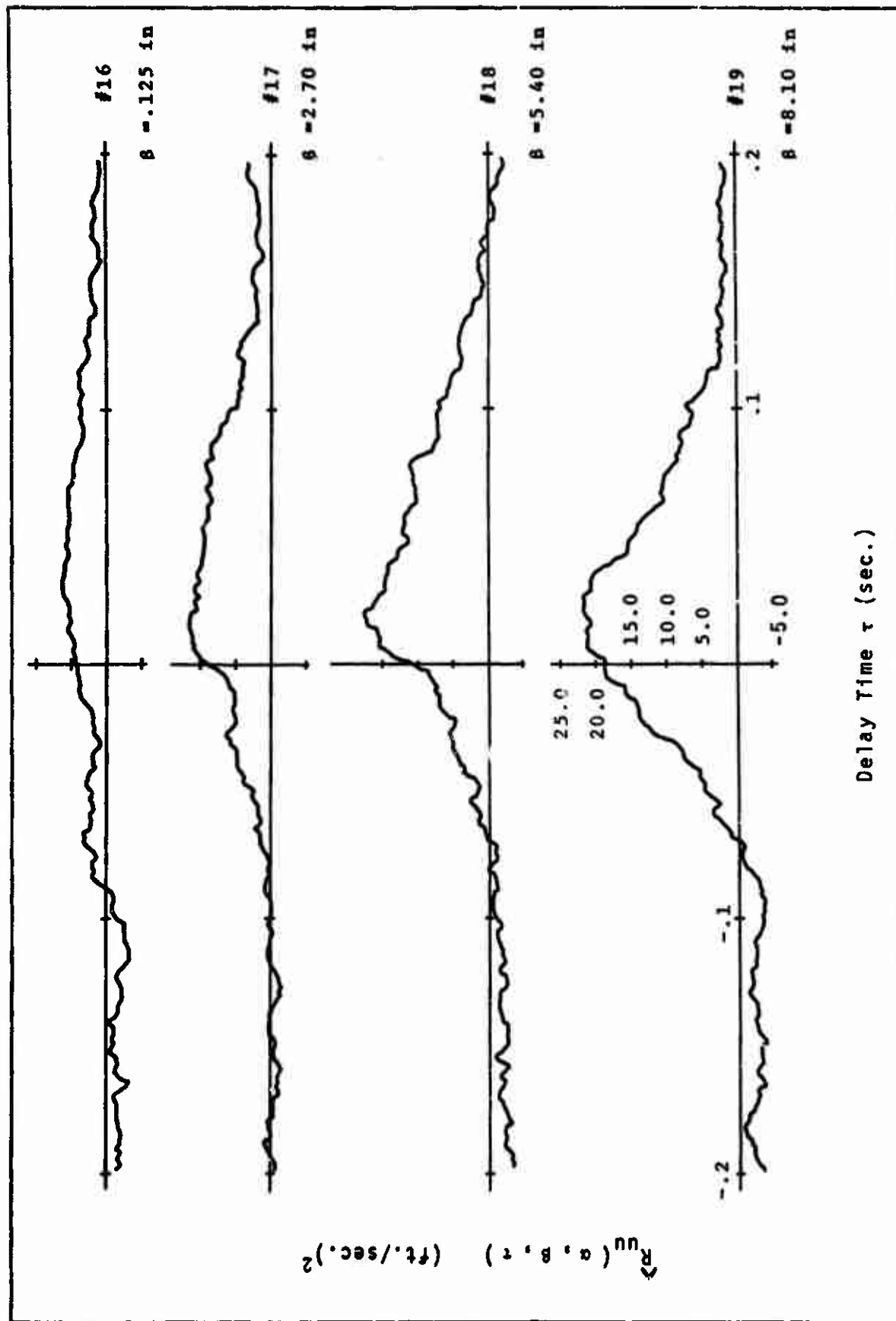


Probe detail

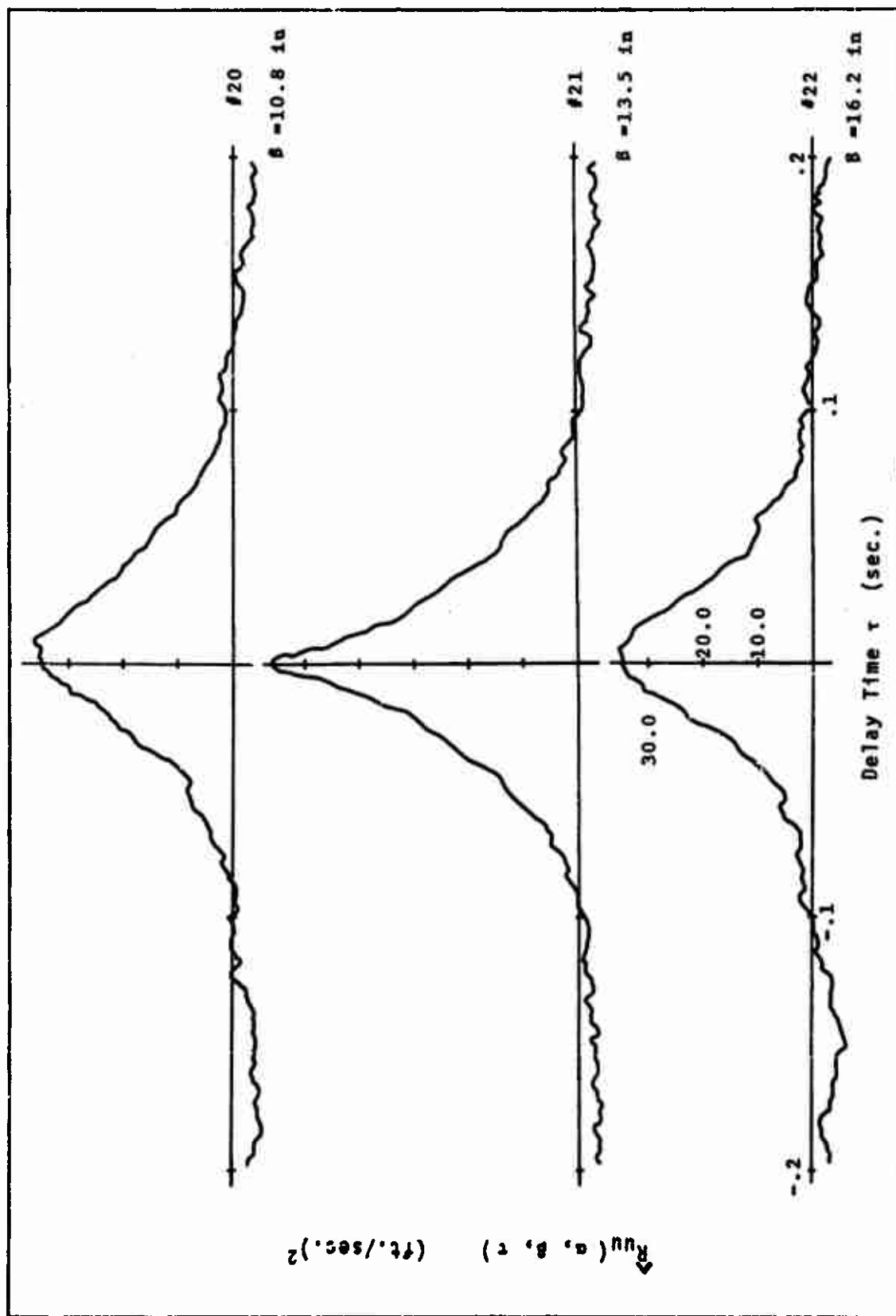


Survey arrangement

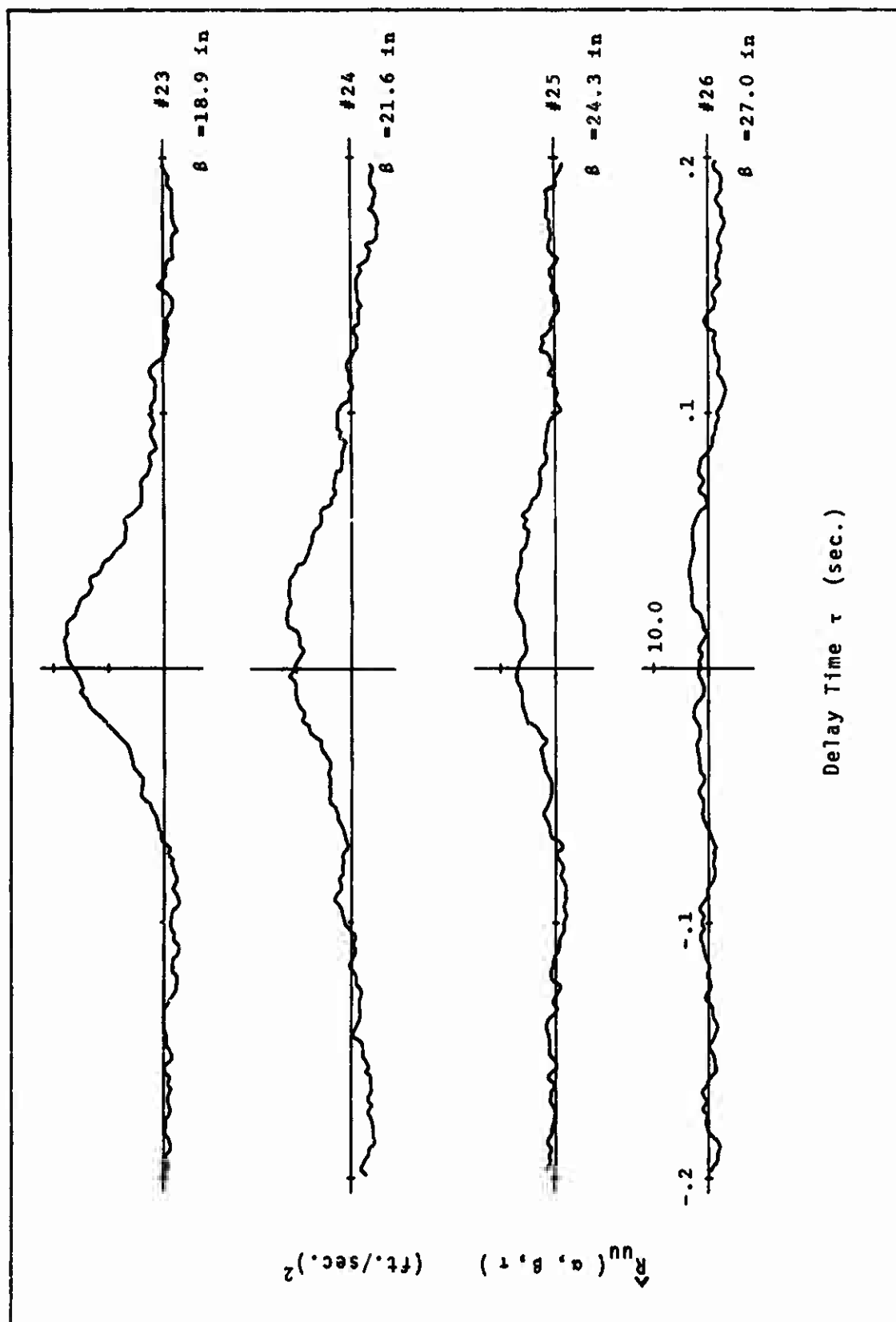
Fig.15 - HOT WIRE PROBES



Figs.16-19 - SPACE-TIME CORRELATION COEFFICIENTS



Figs.20-22 - SPACE-TIME CORRELATION COEFFICIENTS



Figs.23-26 - SPACE-TIME CORRELATION COEFFICIENTS

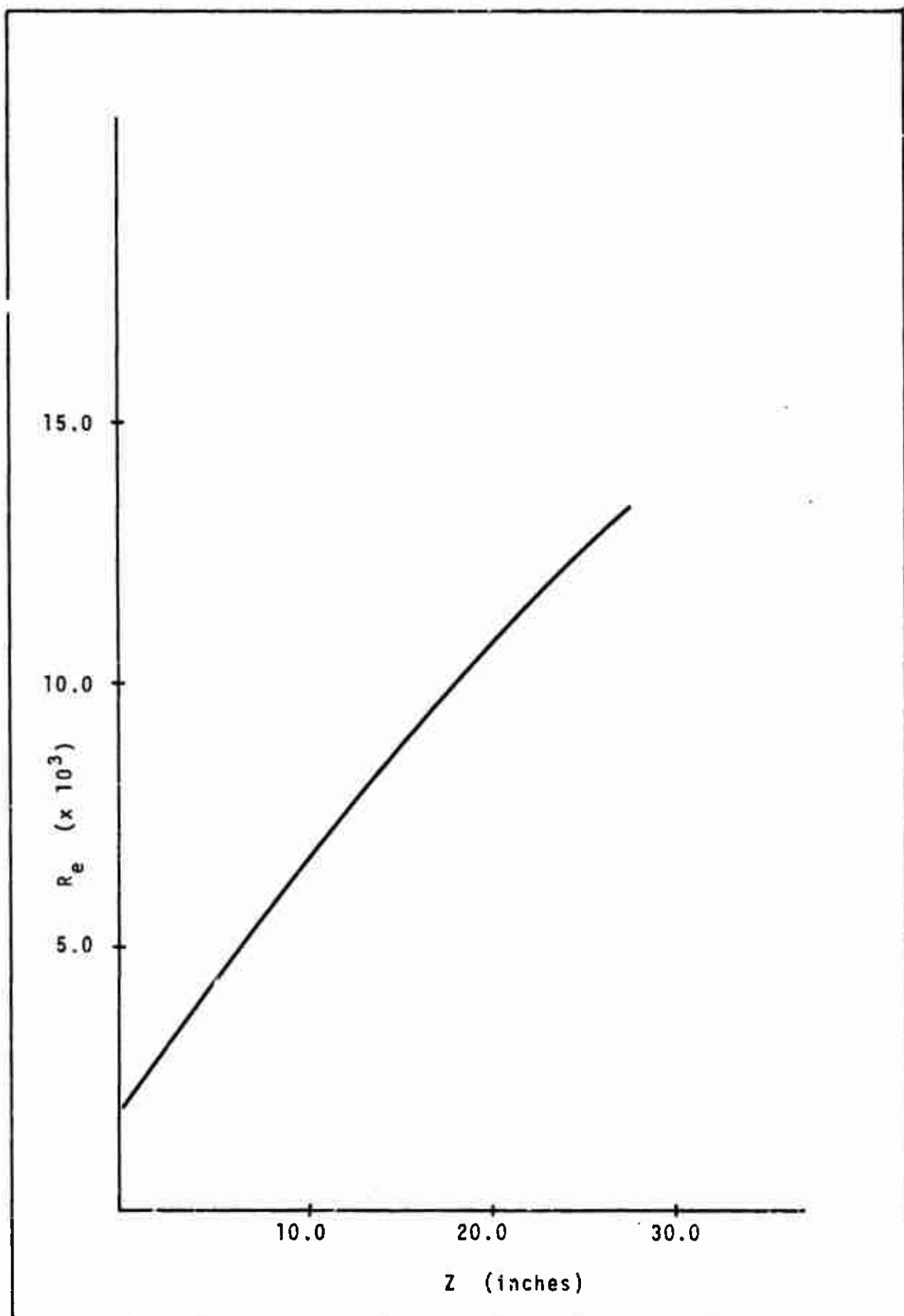
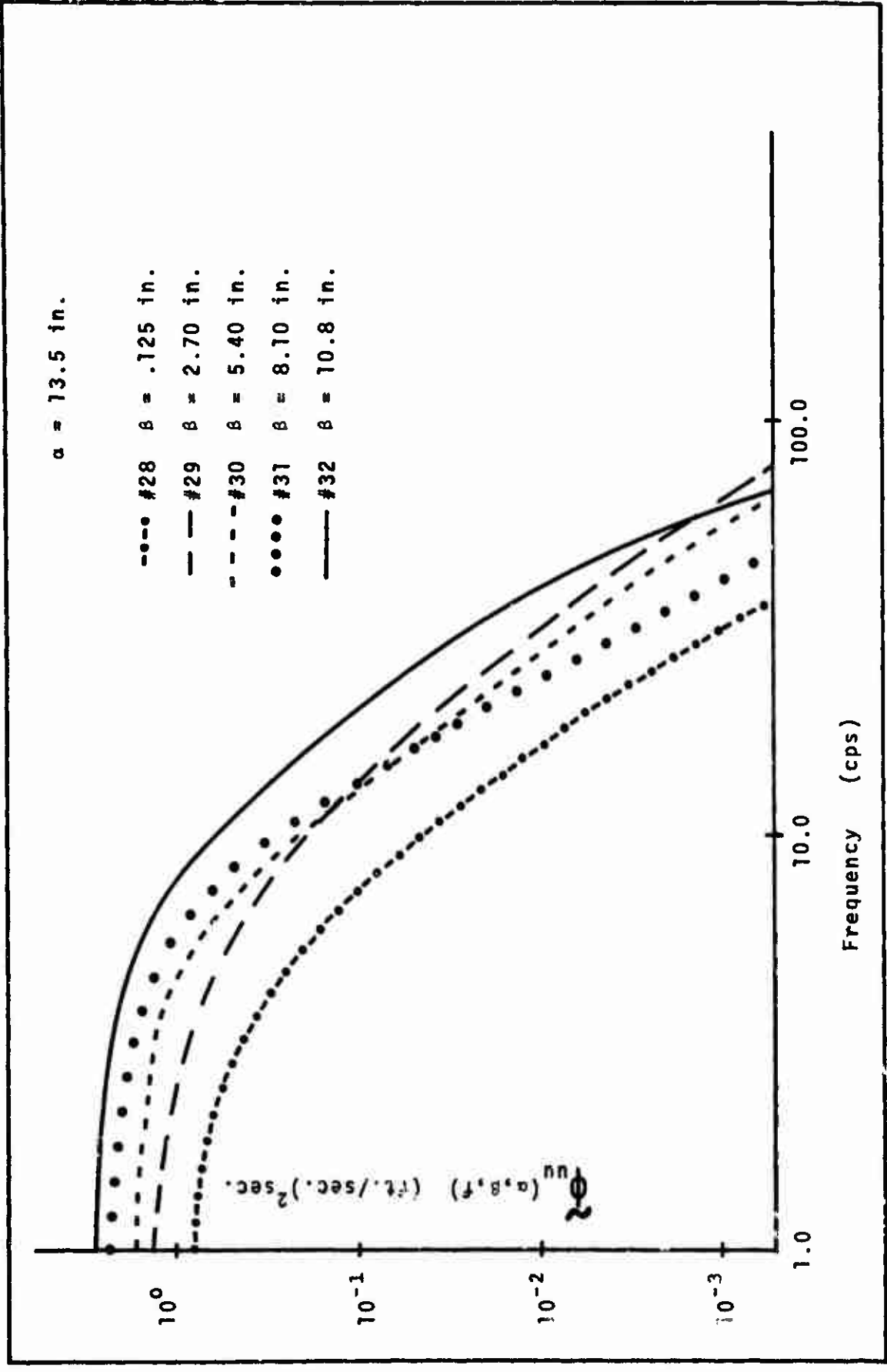


Fig.27 - REYNOLD'S NUMBER DISTRIBUTION



Figs.28-32 - TURBULENCE CROSS SPECTRA

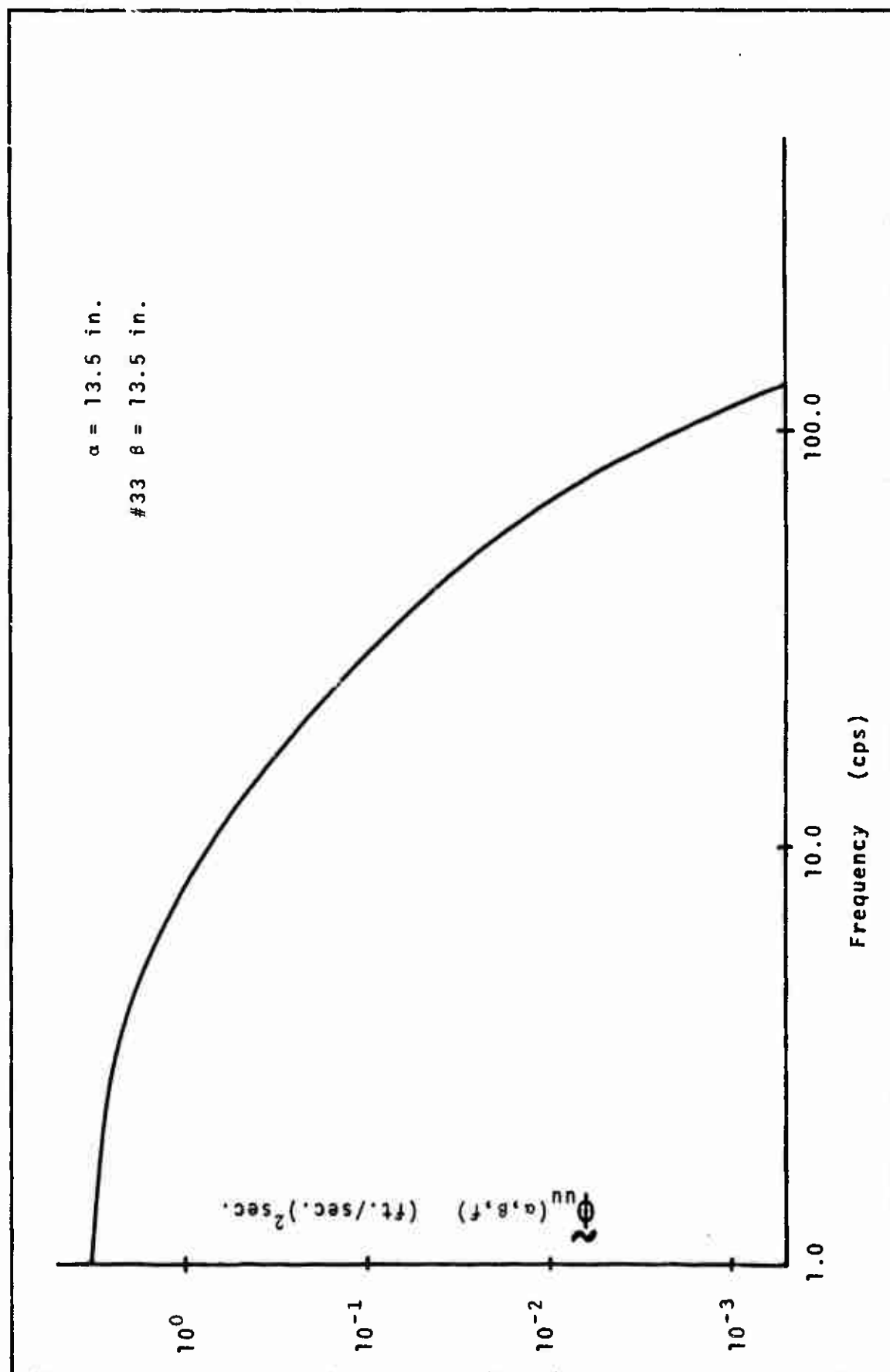
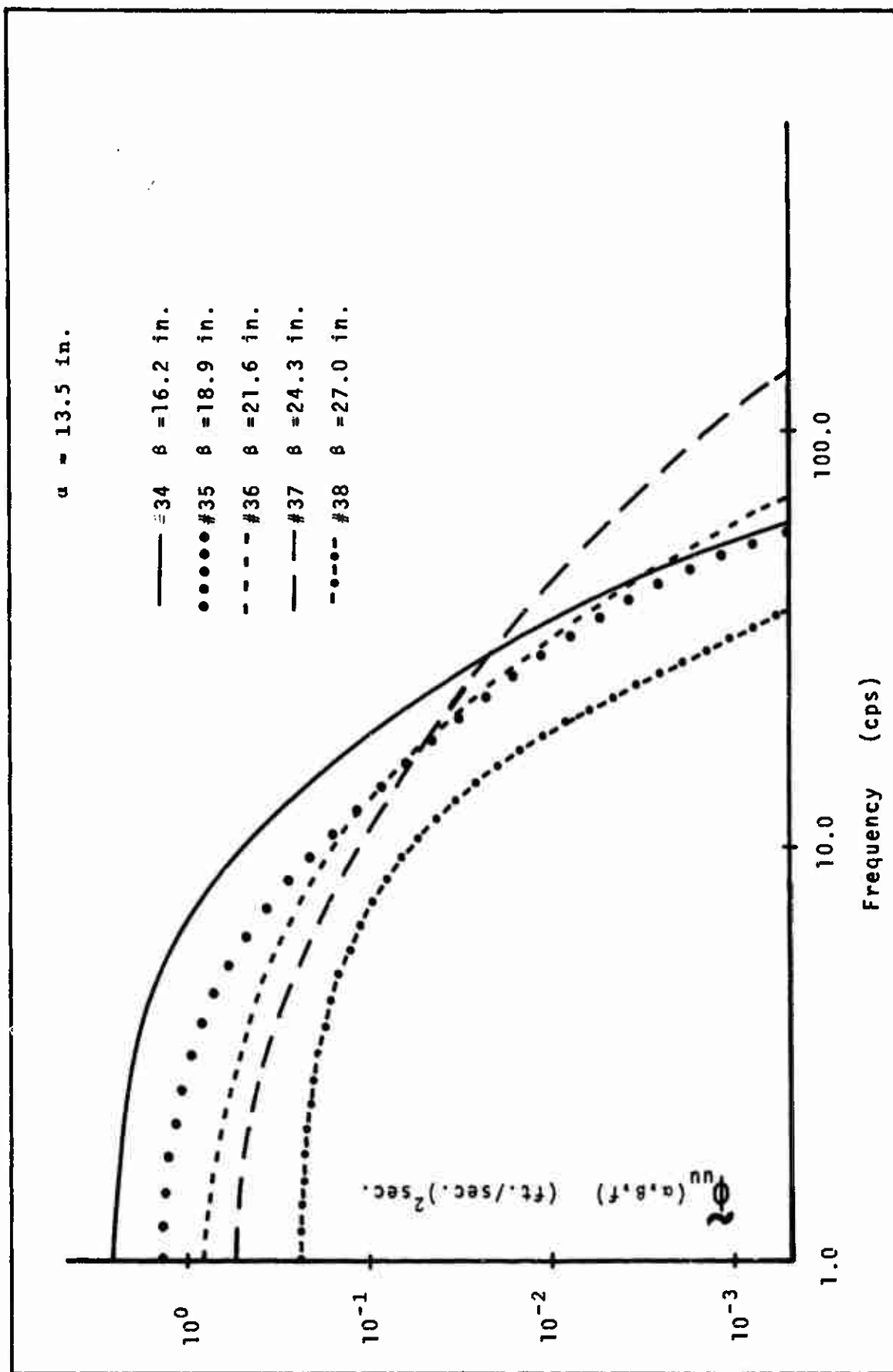


Fig.33 - TYPICAL TURBULENCE POWER SPECTRUM



Figs. 34-38 - TURBULENCE CROSS SPECTRA

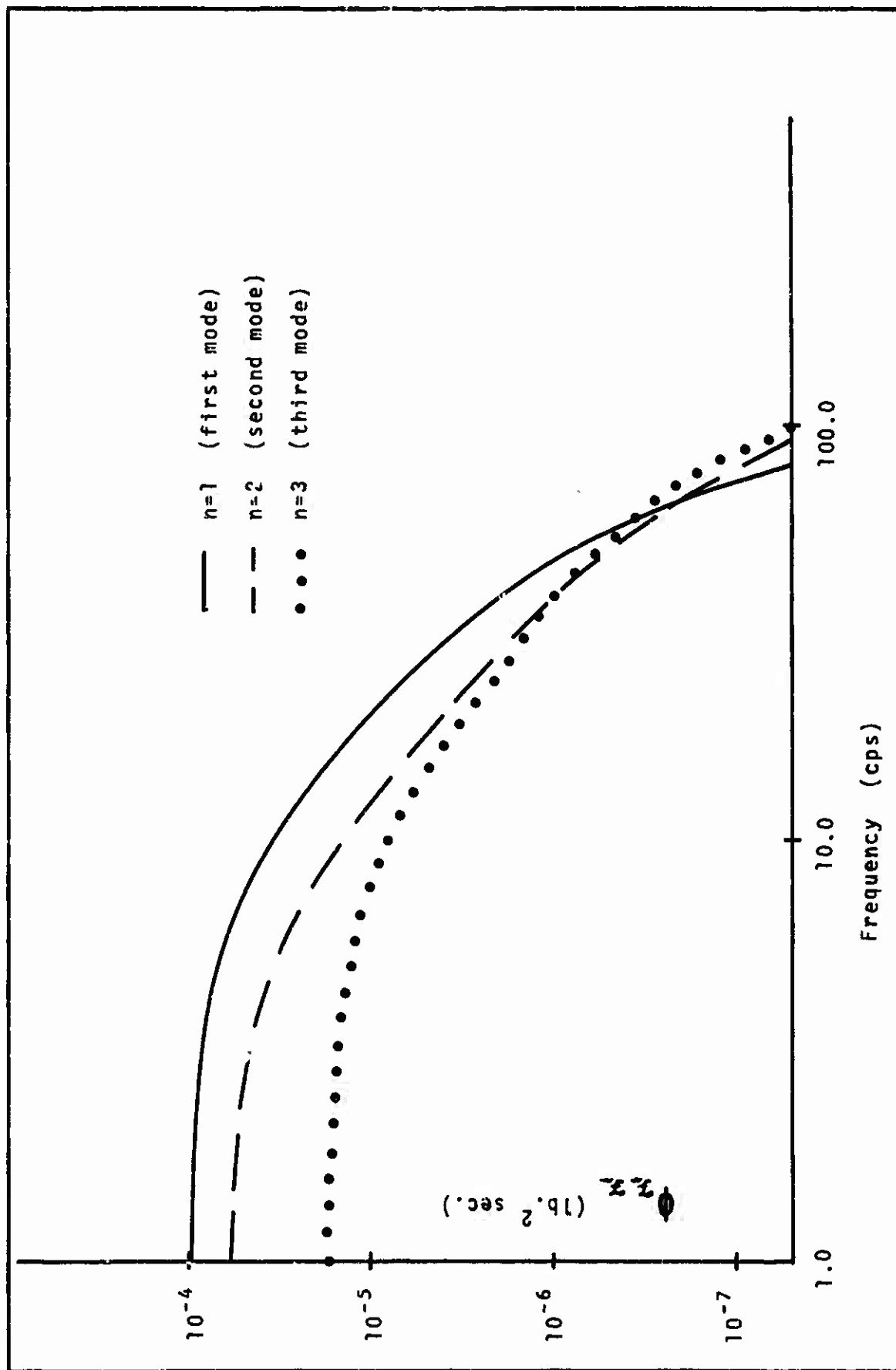


Fig.39 - GENERALIZED INPUT FORCES

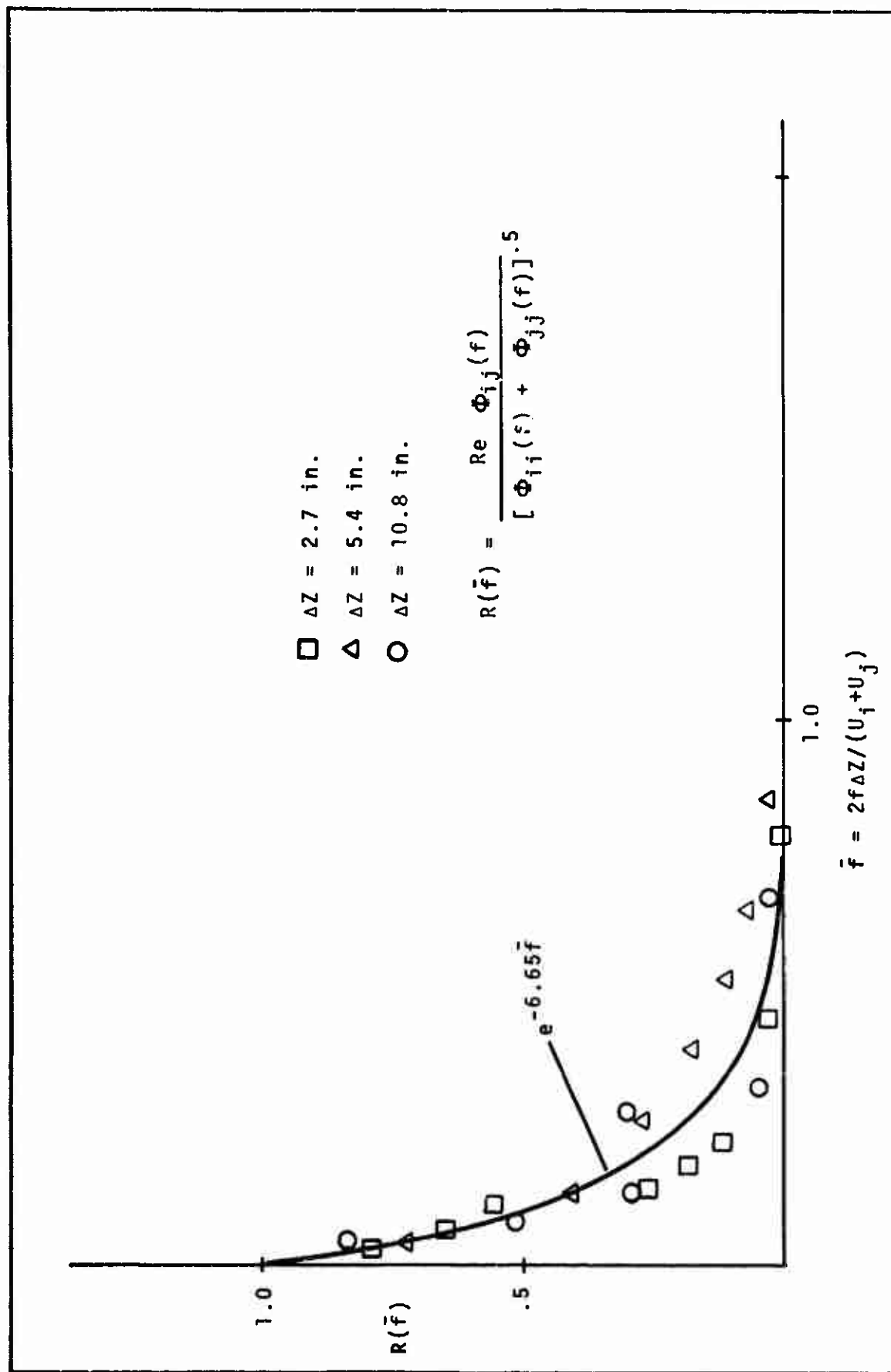
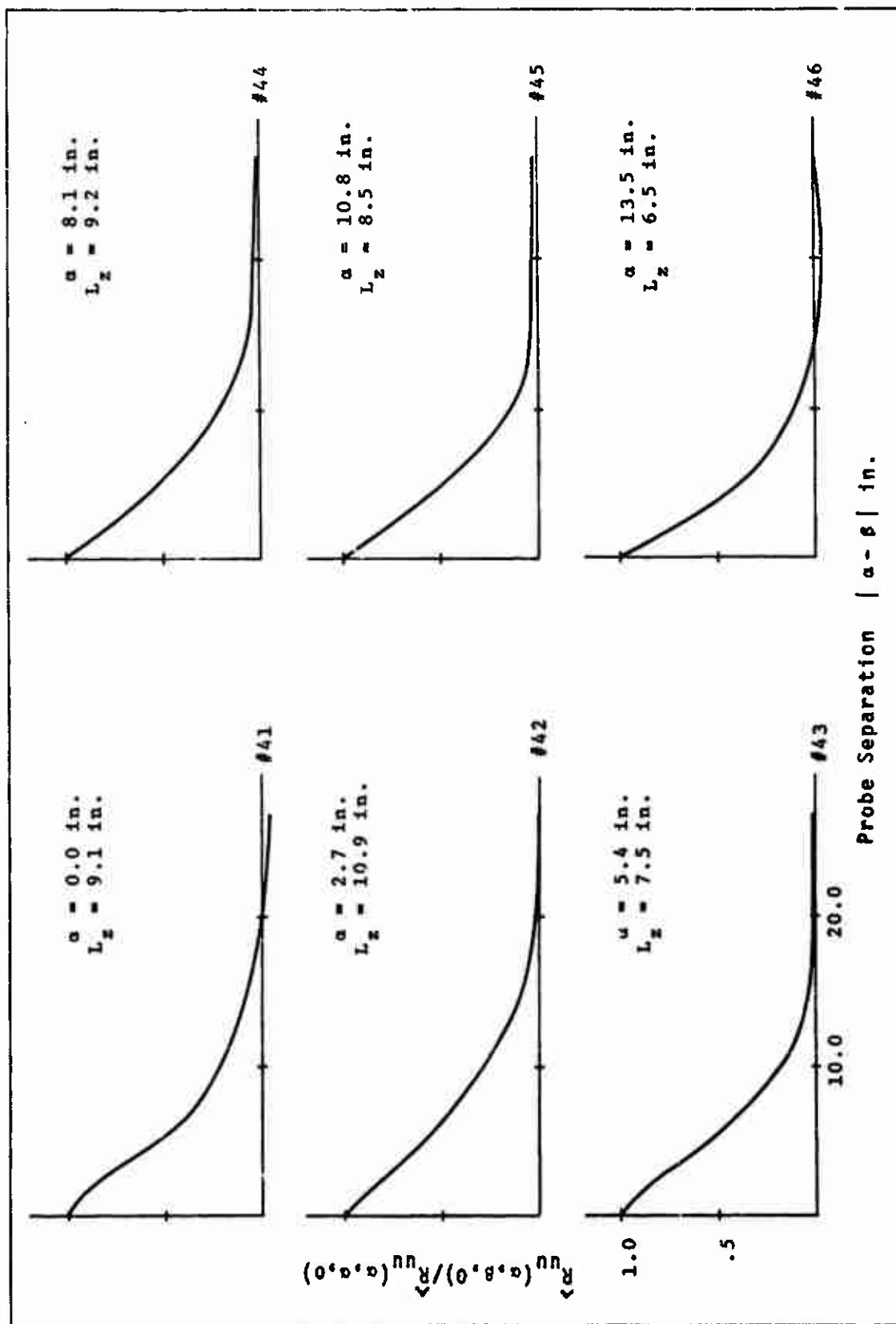
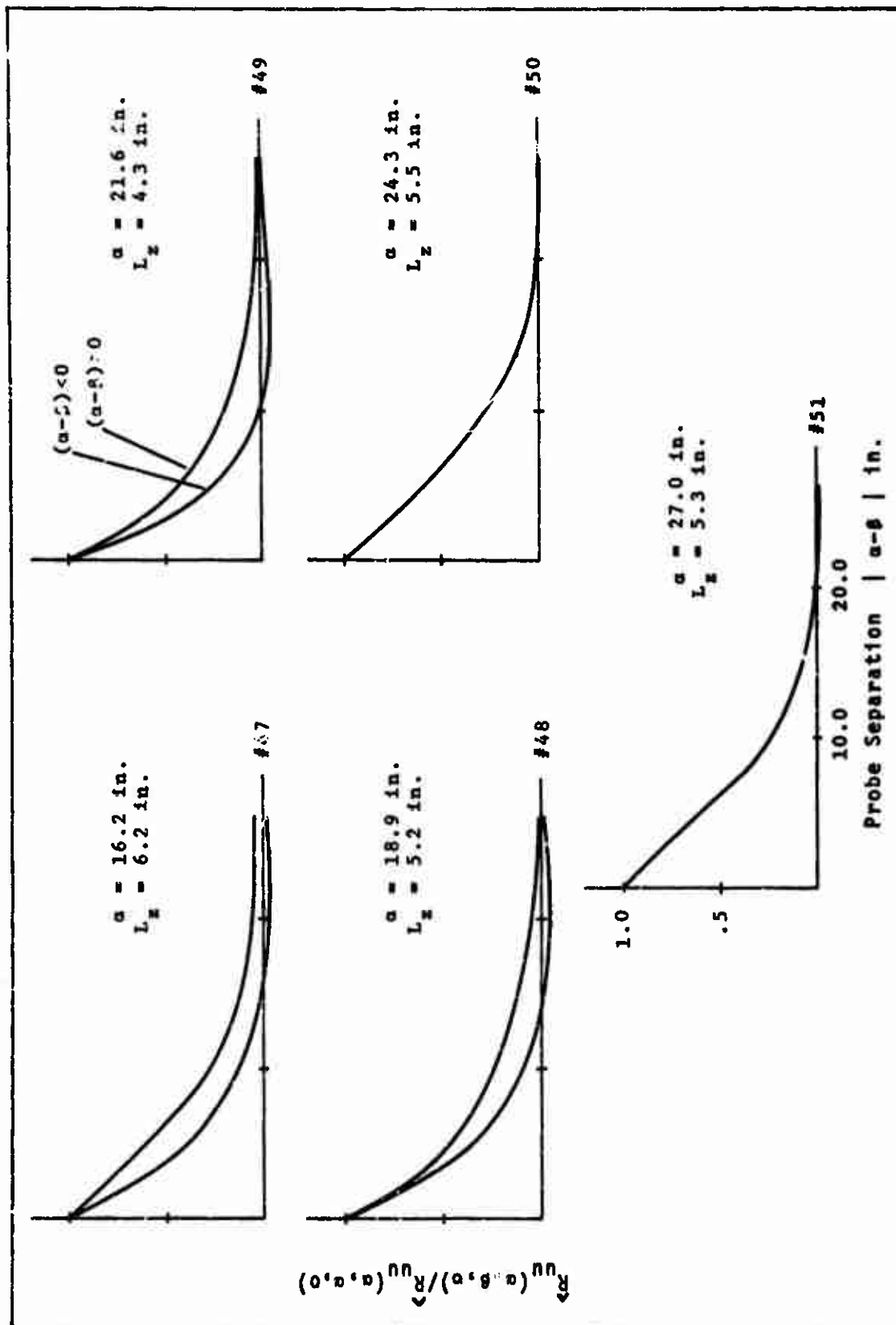


Fig.40 - NARROW BAND CORRELATION FUNCTION



Figs. 41-46 - NORMALIZED CROSS-CORRELATION FUNCTIONS



Figs. 47-51 - NORMALIZED CROSS-CORRELATION FUNCTIONS

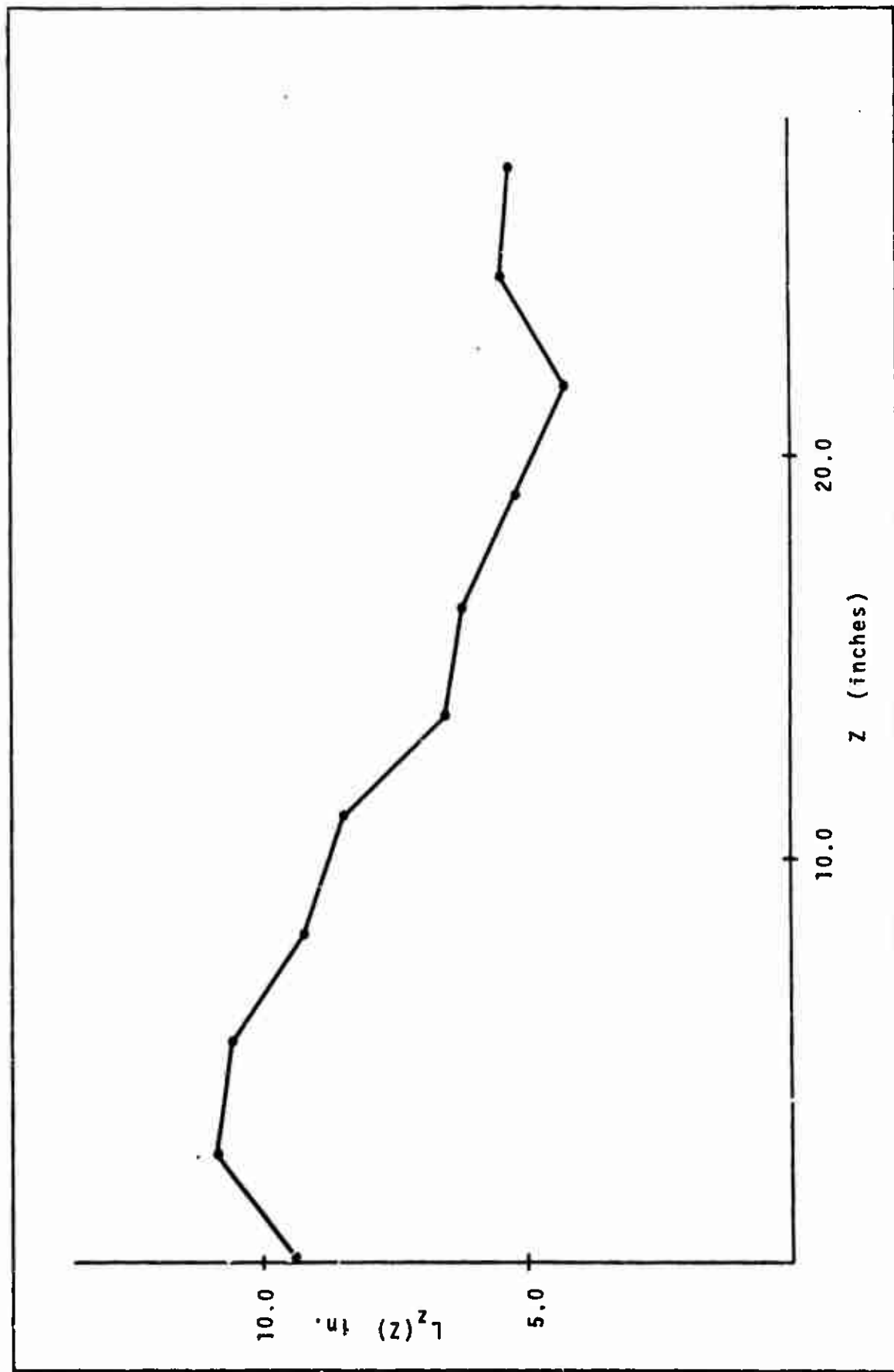


Fig.52 - LATERAL INTEGRAL SCALE

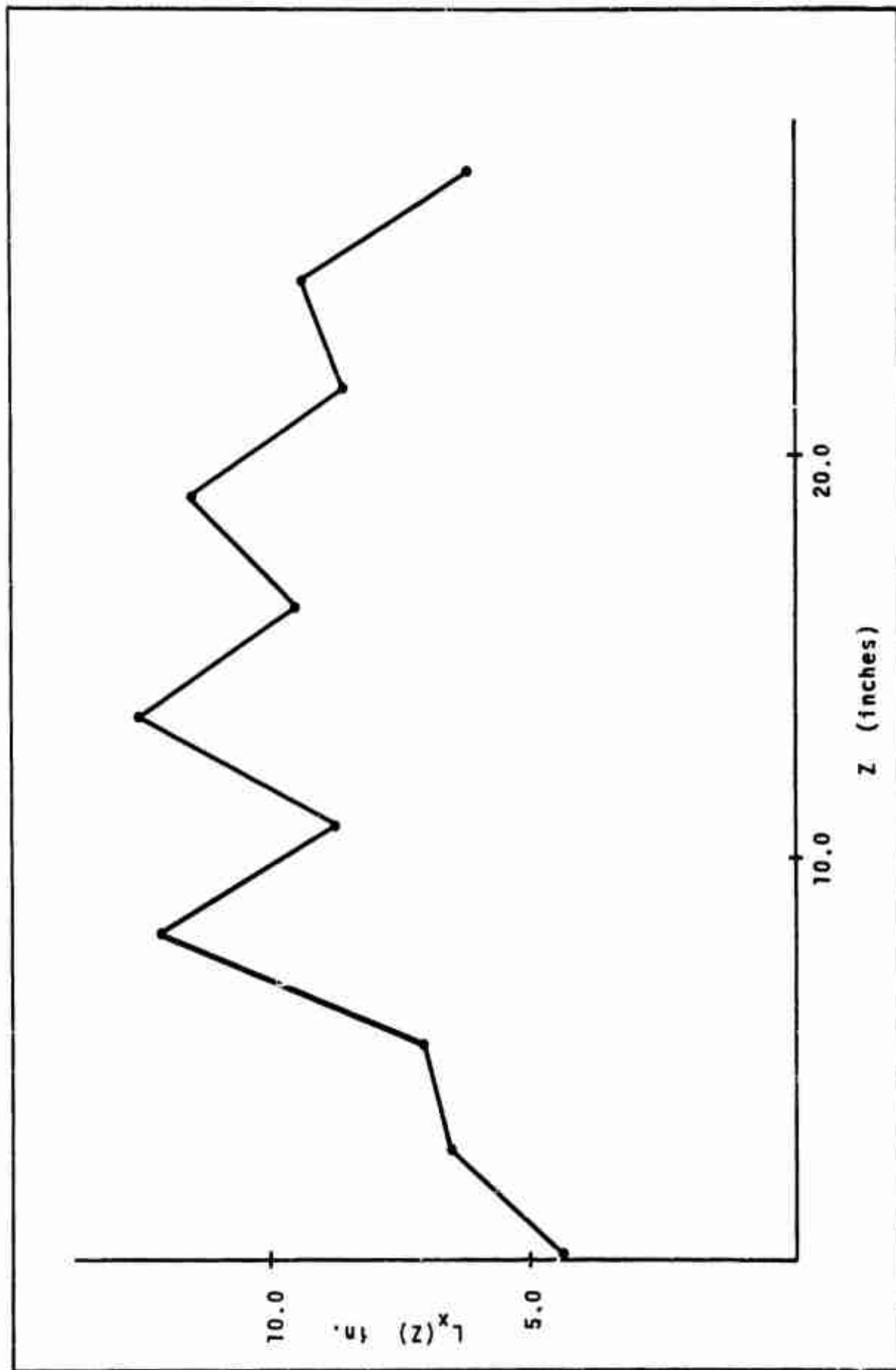


Fig.53 - LONGITUDINAL INTEGRAL SCALE

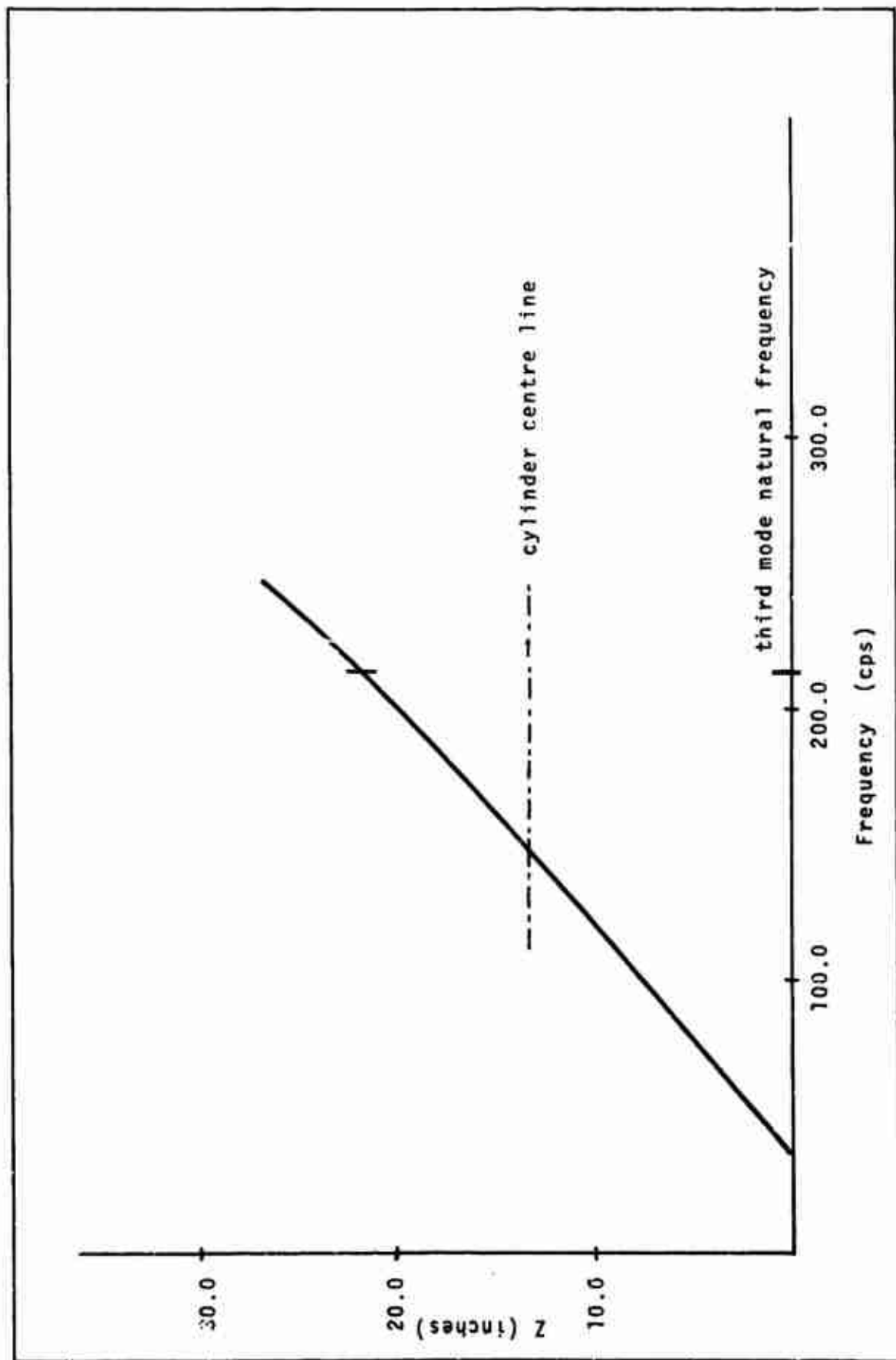


Fig.54 - STROUHAL VORTEX SHEDDING FREQUENCY

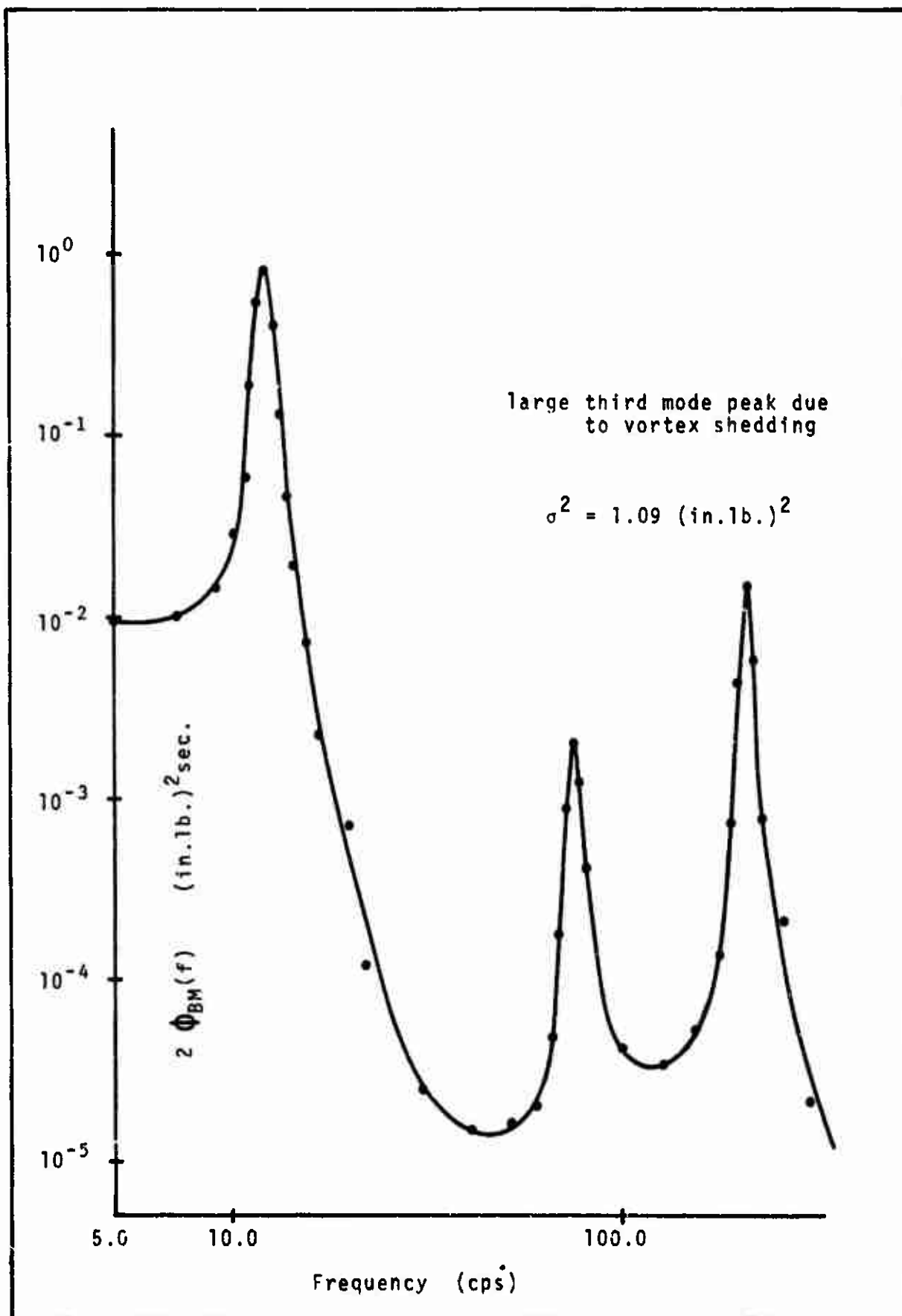


Fig.55 - EXPERIMENTAL LIFT BENDING MOMENT SPECTRAL RESPONSE

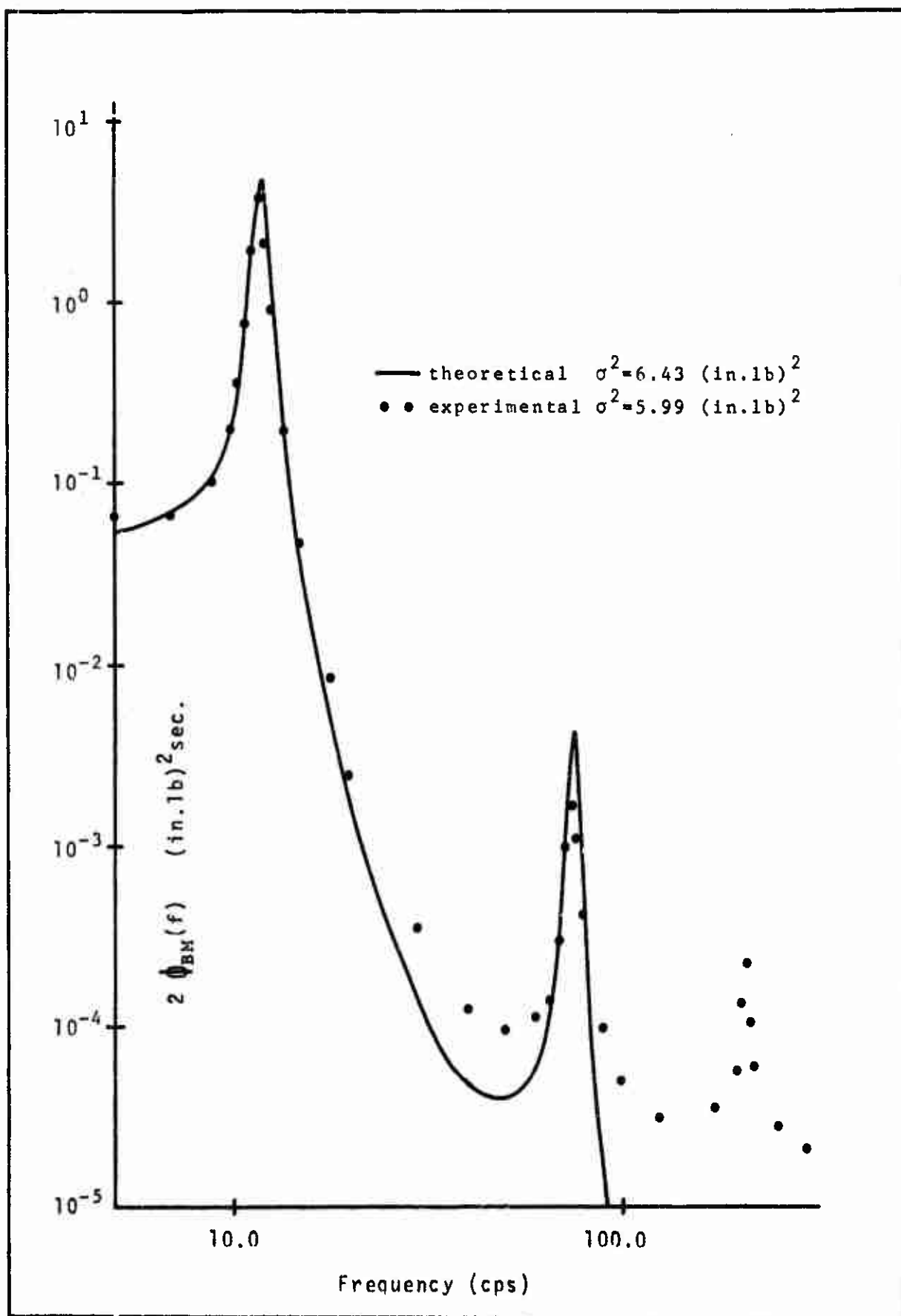


Fig.56 - COMPARISON OF FILTERED THEORETICAL AND EXPERIMENTAL SPECTRA

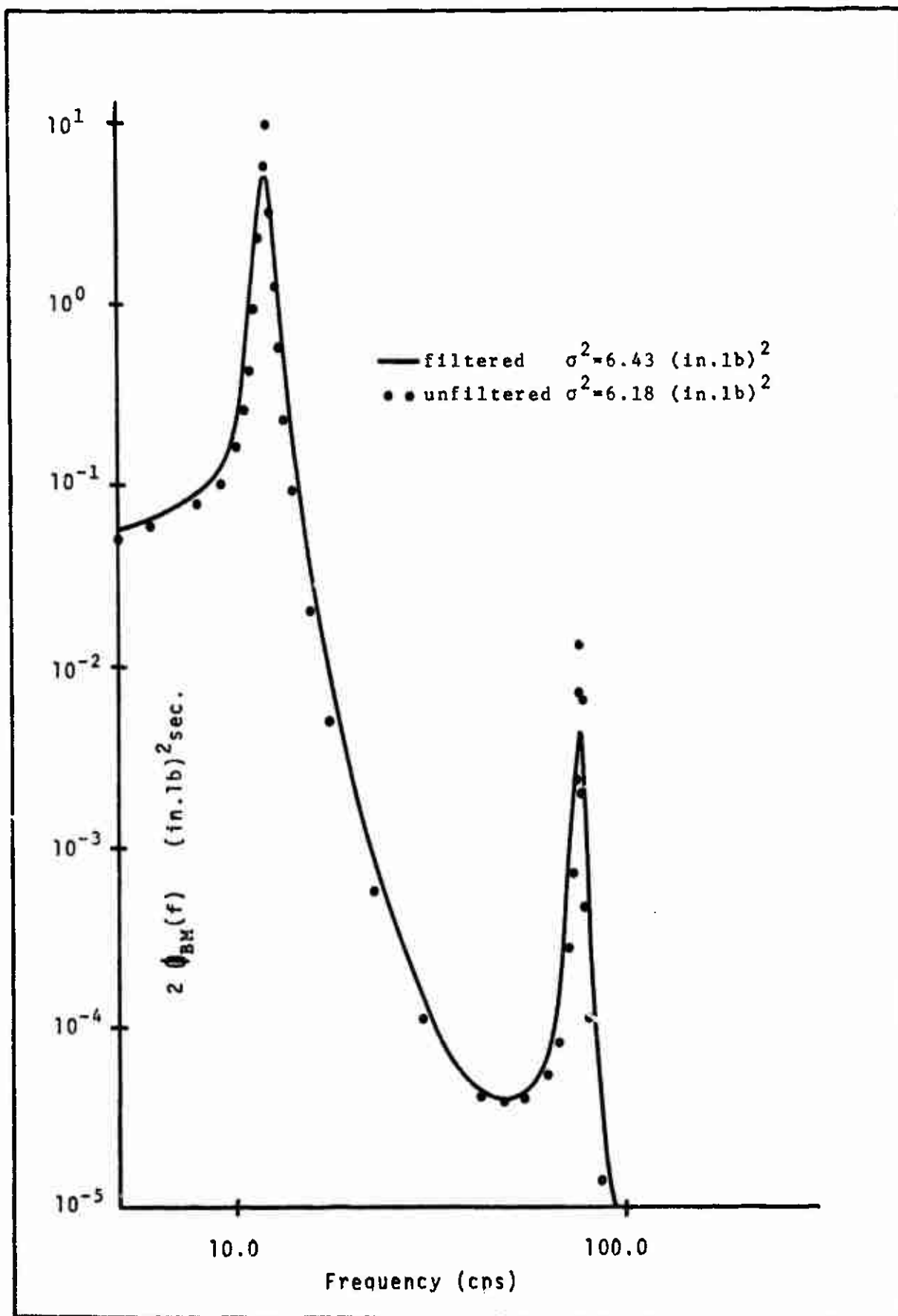


Fig.57 - COMPARISON OF THEORETICAL FILTERED AND UNFILTERED SPECTRA

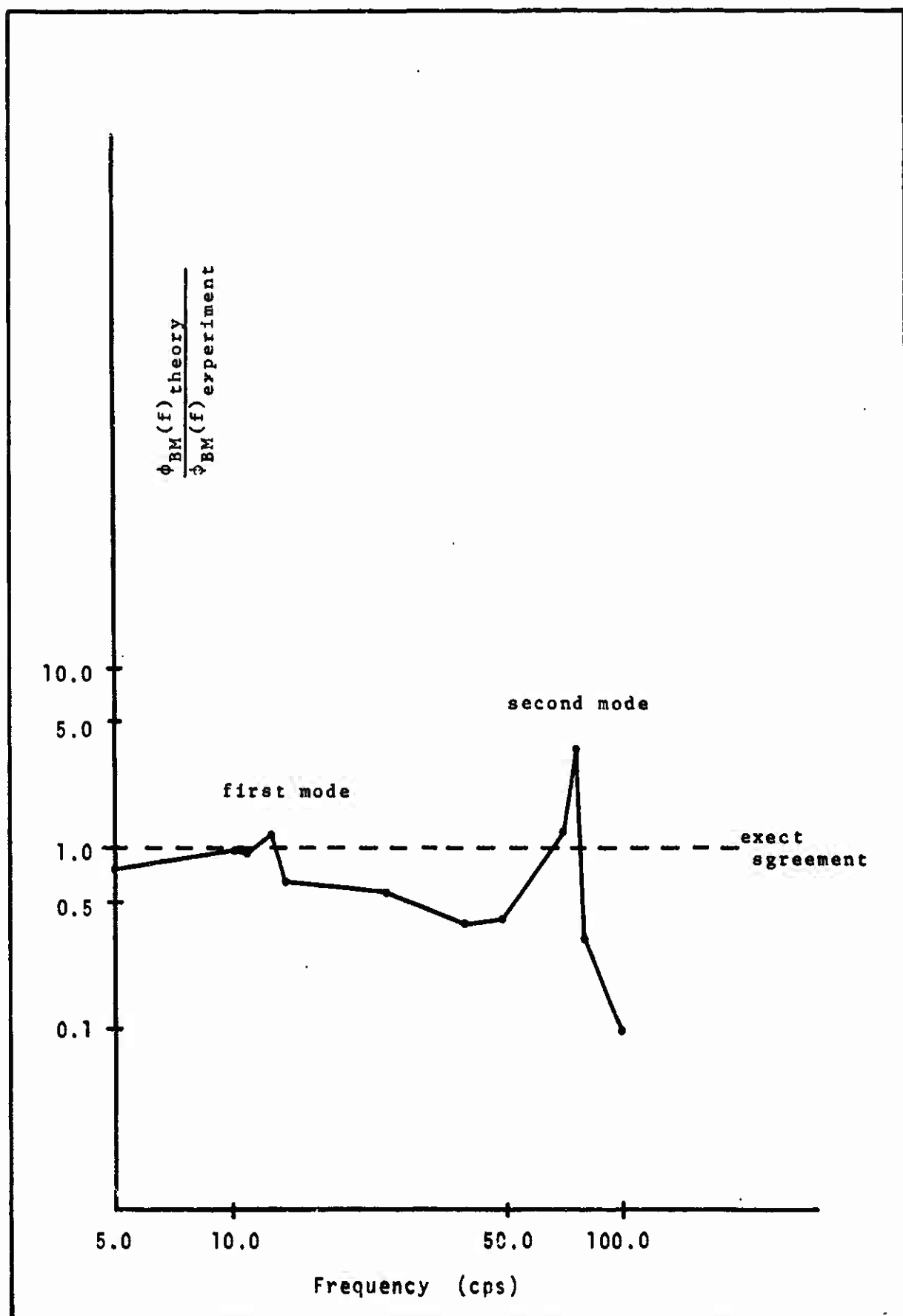


Fig.58 - SPECTRUM COMPARISON

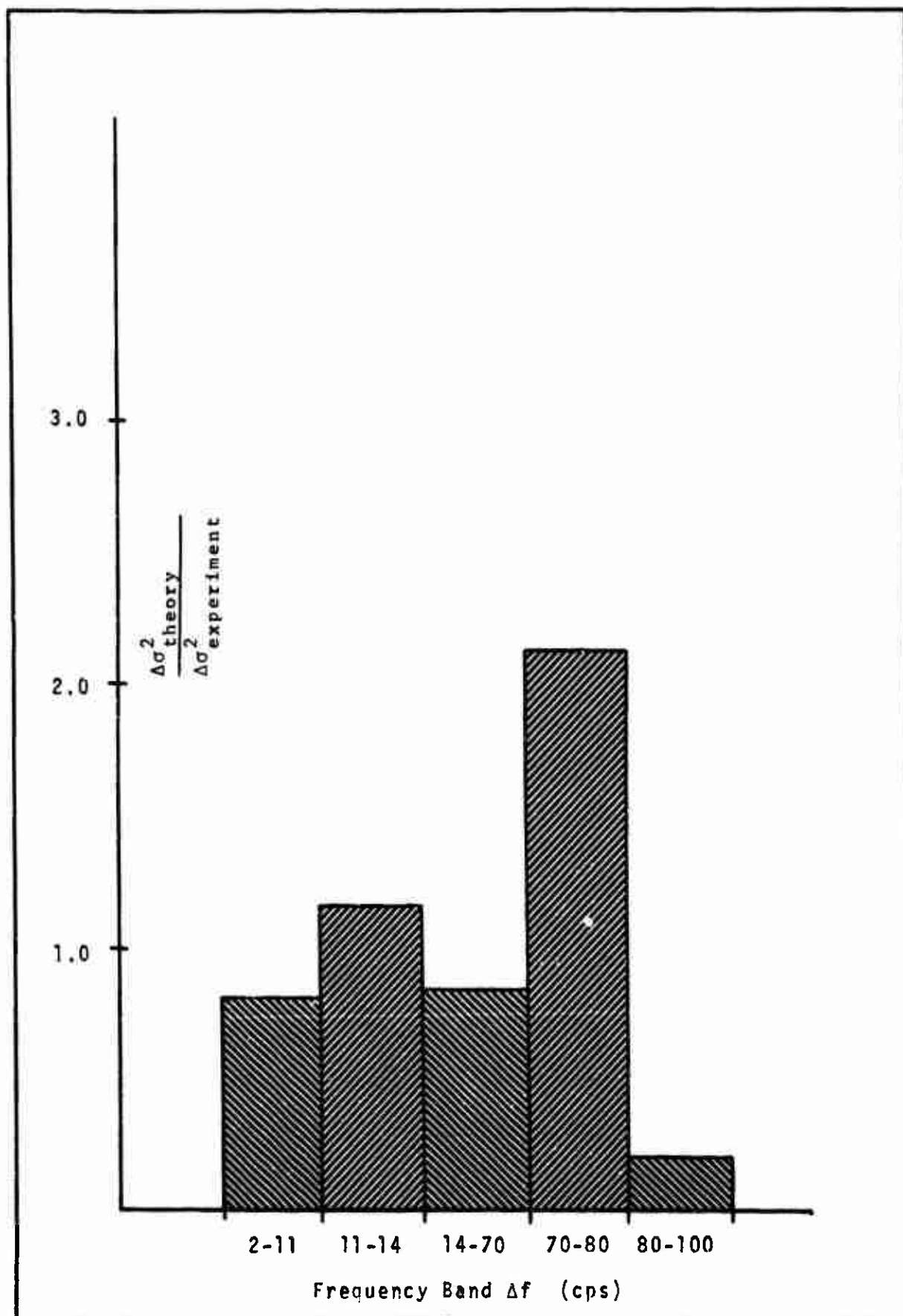


Fig.59 - NARROW BAND VARIANCES

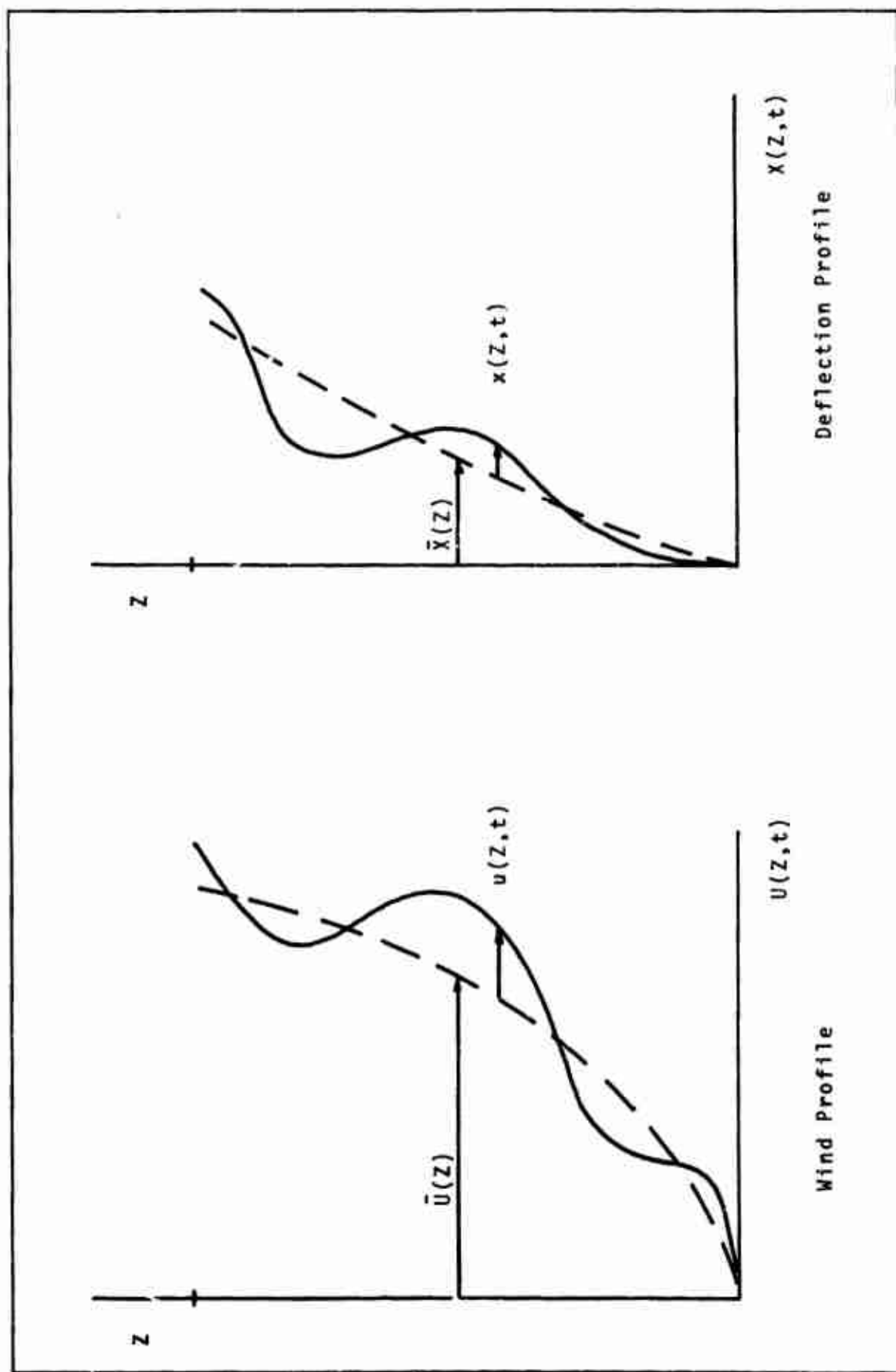


Fig. 60

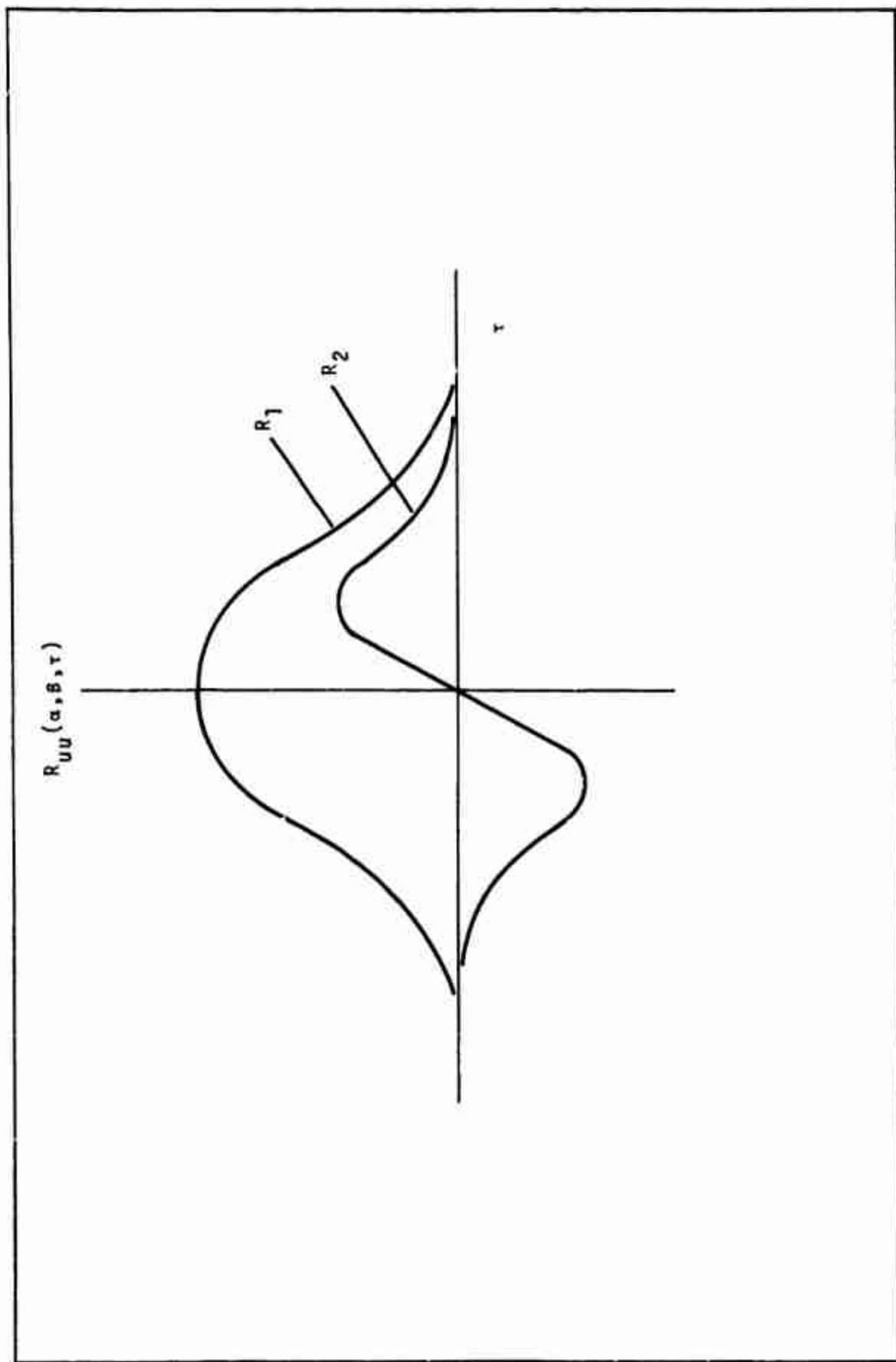


Fig.61 - SYMMETRIC AND ANTISYMMETRIC COMPONENTS OF THE CORRELATION FUNCTION

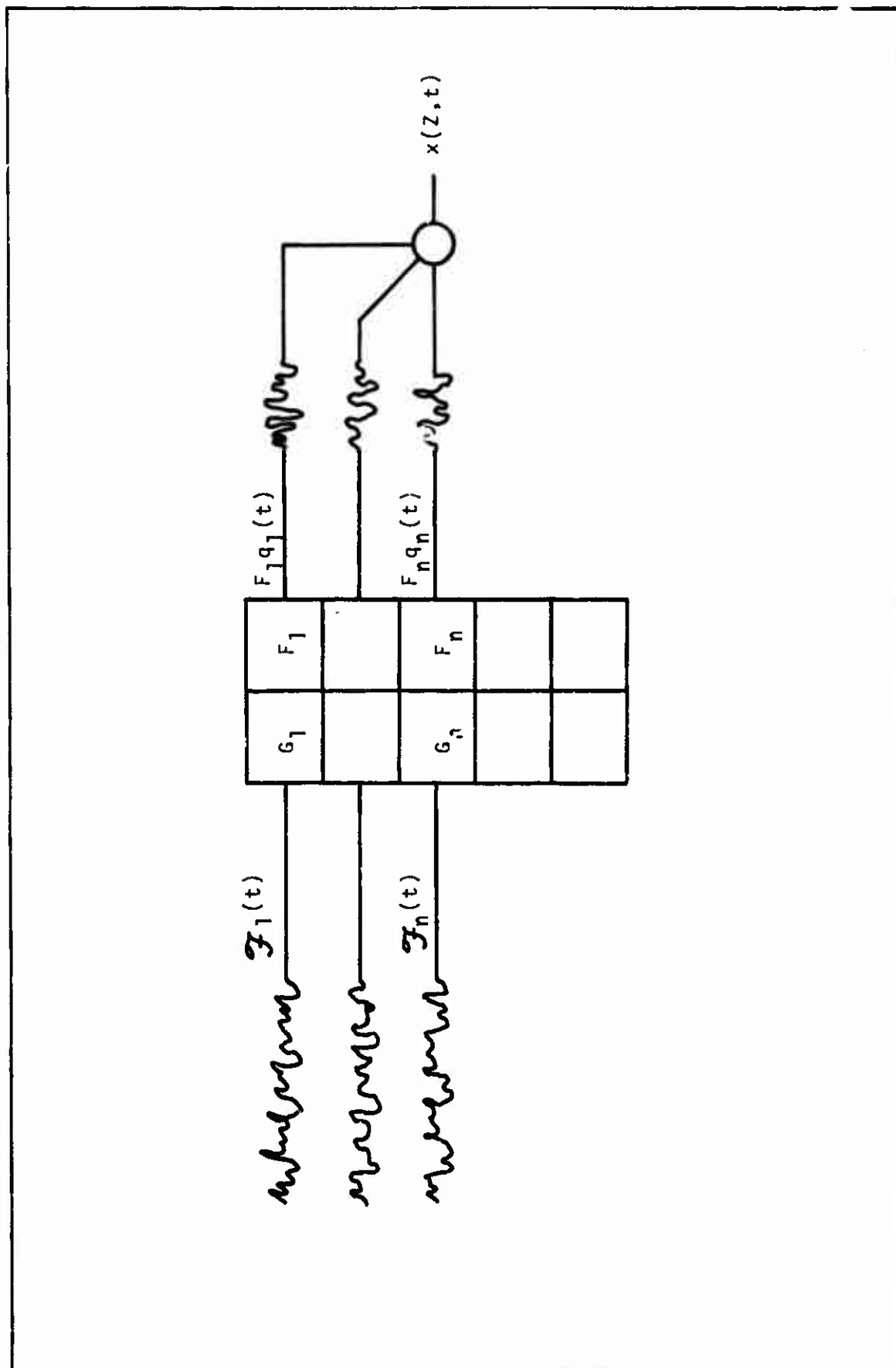


Fig.62 - SUPERPOSITION OF MODEL RESPONSES

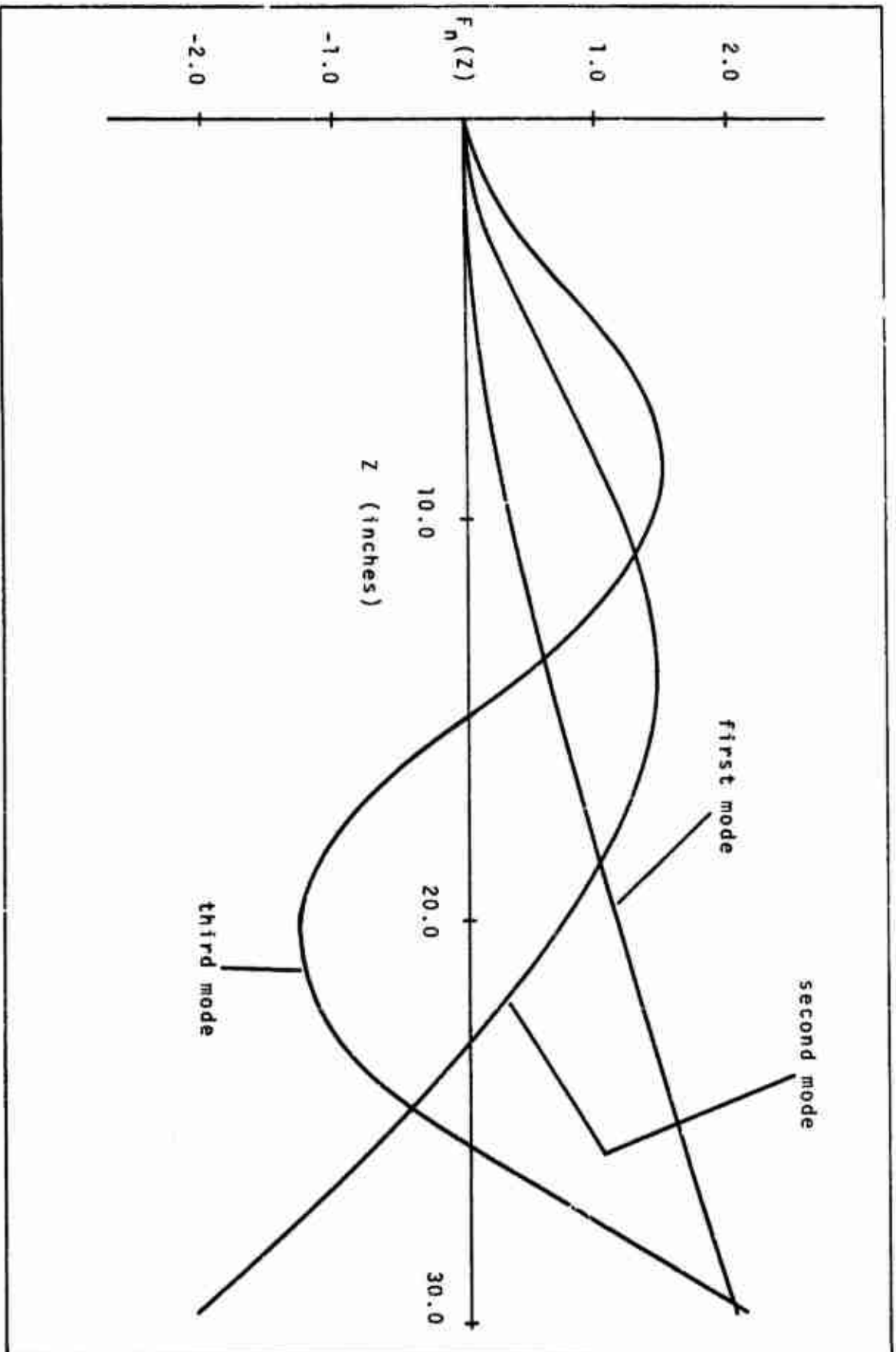


Fig. 63 - CANTILEVER CYLINDER MODE SHAPE FUNCTIONS

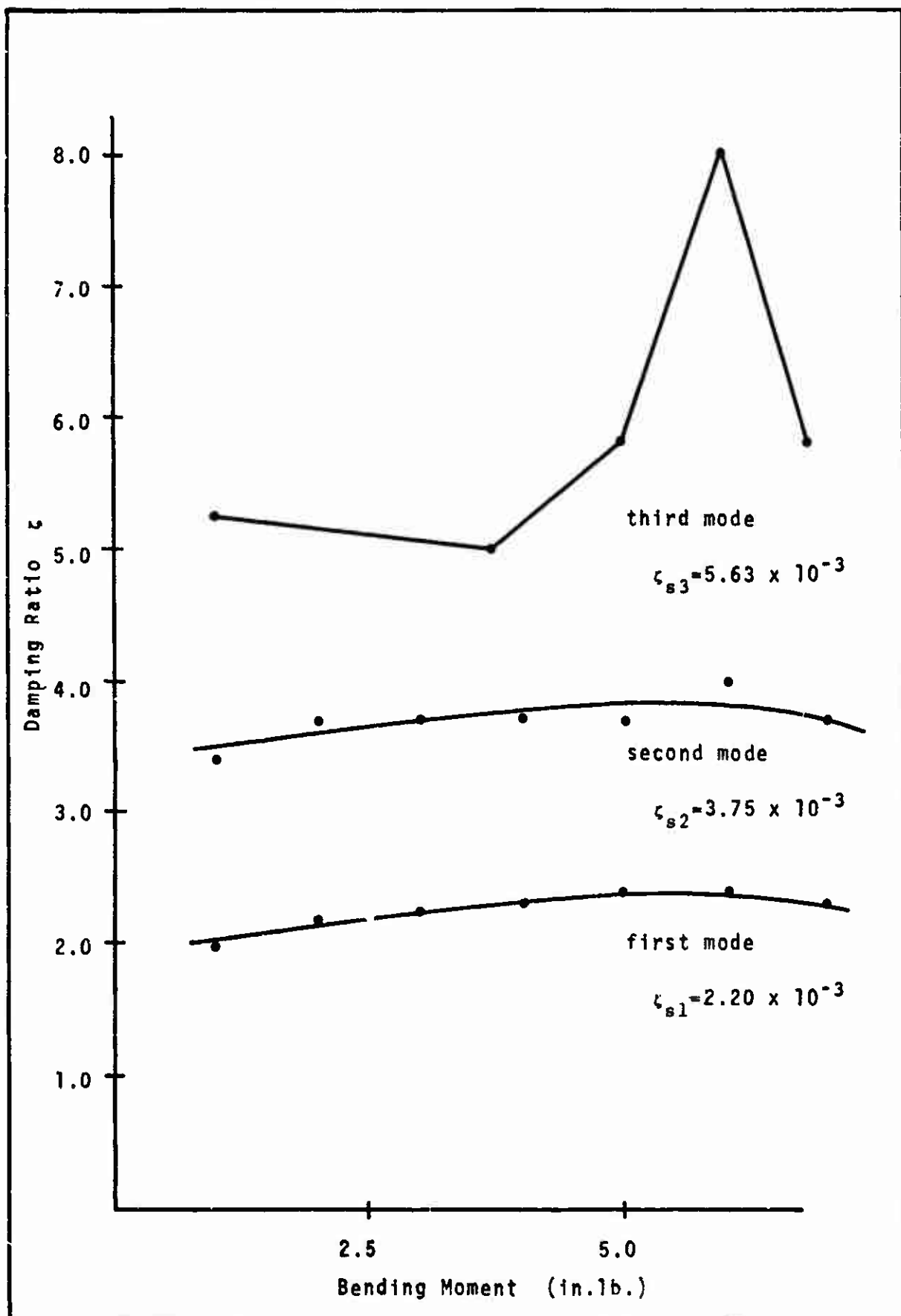


Fig.64 - STRUCTURAL DAMPING

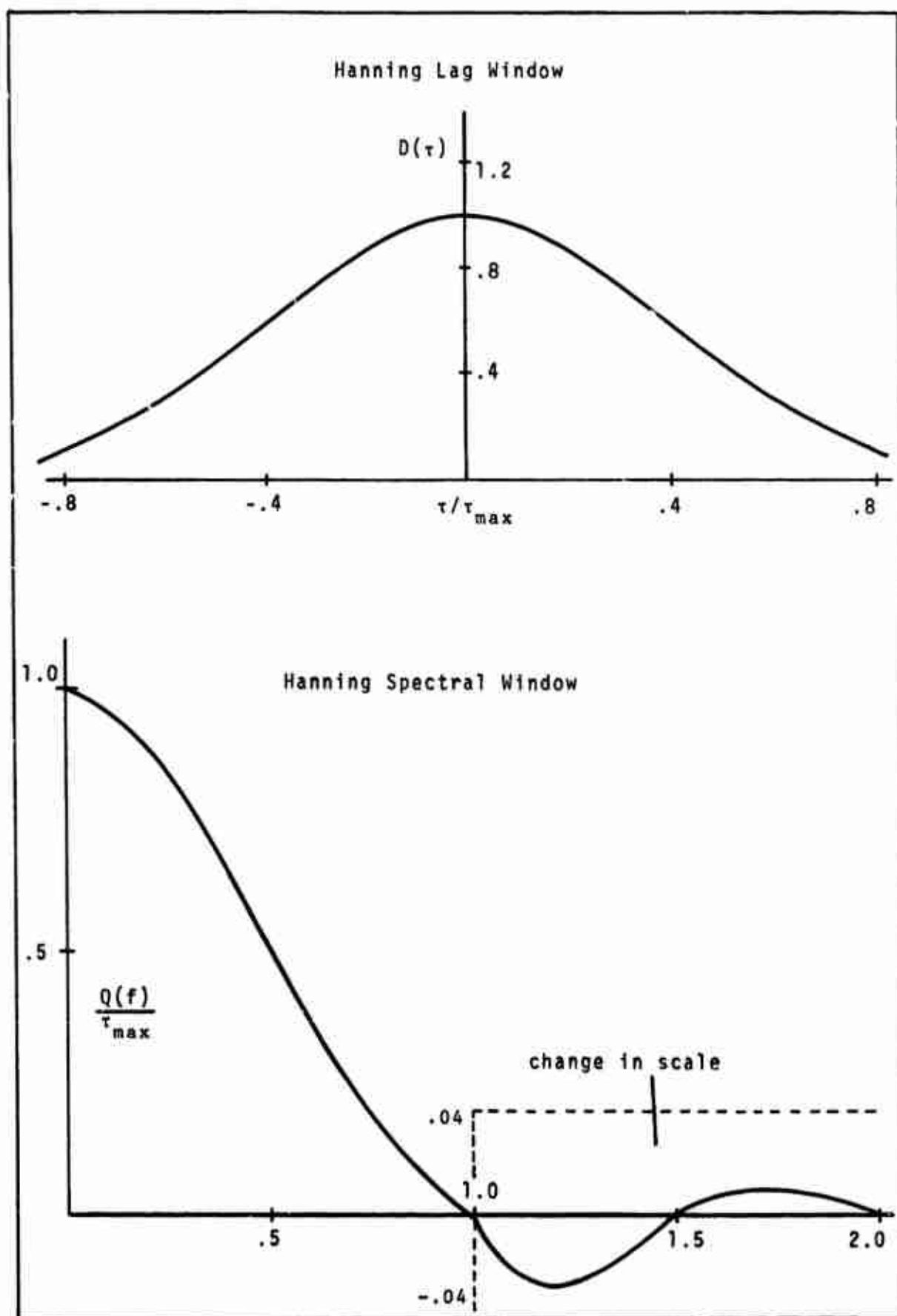


Fig.65

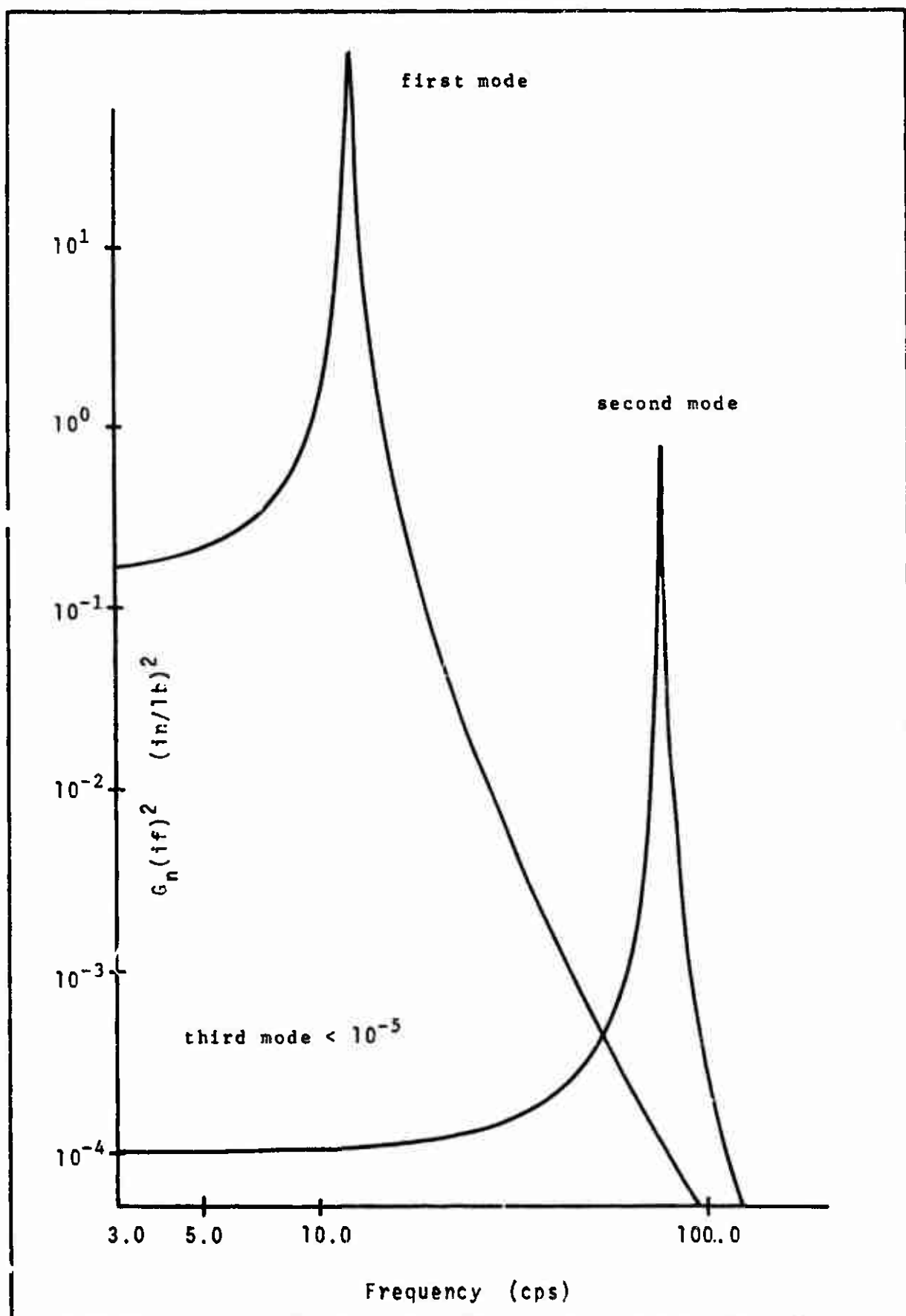
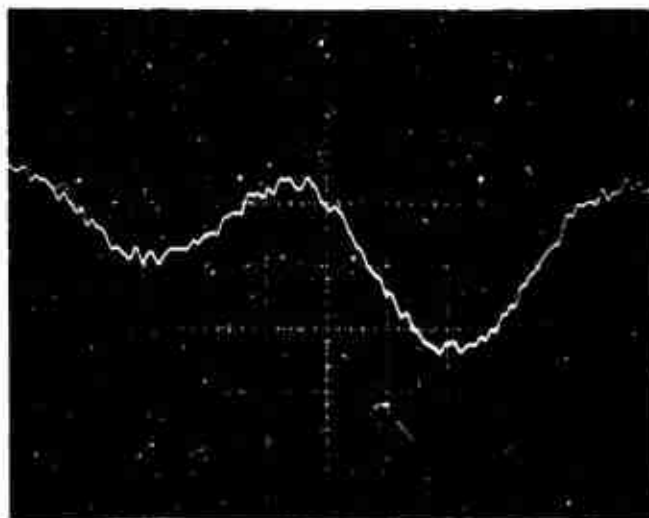
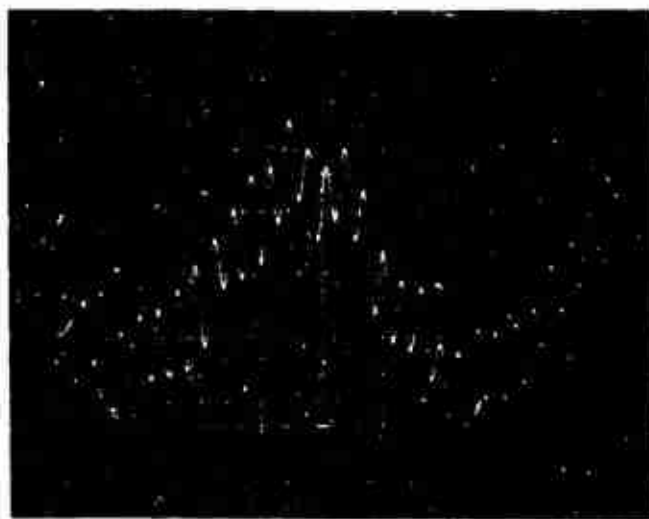


Fig.66 - SYSTEM TRANSFER FUNCTIONS



Drag signal



Lift signal

Fig.67 - CYLINDER STRAIN GAUGE OUTPUTS